Design and realization of a one-dimensional vibration isolation setup for floor vibrations

Xiaohu Guo

Master's thesis

July 2005

University of Twente
The Netherlands

Faculty of Electrical Engineering, Mathematics and Computer Science
Department of Electrical Engineering
Control Laboratory

Master's thesis in Electrical Engineering
July 2005

University of Twente
Department of Electrical Engineering
Control Laboratory
P.O. Box 217
7500 AE Enschede
The Netherlands

Report no. 026CE2005

Committee:

prof. dr. ir. J. van Amerongen (Universiteit Twente)
prof. ir. H. Soemers (Universiteit Twente)
dr. ir. J. van Dijk (Universiteit Twente)
dr. ir. T.J.A. van Vries (Universiteit Twente)
ir. G. W. van der Poel (Universiteit Twente)

Typeset by the author with the LaTeX 2_ε document preparation system.
Printed in The Netherlands.

Never wait till regret.

- TJ -

Abstract

Nowadays, high precision machines have gained more and more interest with the remarkable development in the manufacturing of complex integrated circuits (also called ICs or chips). One important issue to ensure the precision of the machines is to reduce the unwanted effect of vibrations, either caused by internal moving parts of the machines or various kinds of external disturbances. Floor vibration is a dominant disturbance. Because of the floor vibrations' low-frequent characteristic, vibration isolation cannot simply rely on the application of passive means. On the other hand, active control in vibration isolation is used more and more. To overcome the disadvantages associated with the soft mounting isolation technique, active mounting technique is proposed in this report.

In this project, a one-dimensional setup is designed and built with special focus on the suspension modes of the setup. To mimic the vibration problem of the high precision positioning machine in industry, resonances are designed at 25 Hz and 80 Hz which respectively represent the machine's supporting suspension and internal suspension. Besides that, we assume a 3 Hz resonance to model the floor suspension. Chapter 2 will elaborate on the setup design process.

The second part of this project is to identify the setup dynamics and implement the designed control strategy. Three different control strategies are discussed: classic fixed gain feedback, induced mode feedback and adaptive feedforward. The setup's primary and secondary paths are identified with the subspace model identification techniques. The experiment results of applying the classic fixed gain feedback controller indicate 40 dB and 50 dB noise reduction respectively at the two resonances.

Finally, it can be concluded that the goal of design and realization of the one-dimensional demonstration setup for floor-vibration isolation has been successfully accomplished.

Preface

This report is the final step of my nine-month master project at the Mechanical Automation Laboratory of the Department of Mechanical Engineering, University of Twente. The project can mainly be divided into two parts: the first phase is to design a one-dimensional demonstration setup for hard-mounting active isolation purpose, this will be introduced in chapter 2; the second phase is to do the realtime experiments including the system identification and the implementation of the classic fixed gain feedback control strategy. Due to the limited time, only simulations have been carried out for the induced mode feedback and adaptive feedforward control strategies. My fellow student G. H. Boersma will work on a chain project for developing control strategies for the one-dimensional setup.

Xiaohu Guo
Enschede, 27th June 2005

Nomenclature

Latin symbols

Symbol	*Description*
A	cross-section
c_{tilt}	tilting stiffness provided by one branch
$c_{torsion}$	torsional stiffness provided by one branch
C_{tilt}	tilting stiffness provided by one flexure
$C_{torsion}$	torsional stiffness provided by one flexure
C_{TI}	tilting stiffness for one mass
C_{TO}	torsional stiffness for one mass
d	disturbance signal; damping ratio; thickness
e	error signal
E	*Young's modulus*
f_*	suspension resonance for $*$, $* = f, s, i, v$
	resonance caused by mode $*$, $* = 1, 2, 3$
$f_{criterion}$	critical frequency
f_s	sample frequency
F_a	force supplied by the piezo-actuator
F_f	excitation force for the primary path
h	width of one branch in a guiding flexure
I	second moment of inertia
I_g	polar moment of inertia of masses in **x** or **y** direction
I_j	polar moment of inertia of masses in **z** direction
k_*	stiffness, $* = 1, 2, 3, 4, i$
k_{23}	equivalent stiffness for k_2 and k_3 in series
k_g	stiffness in longitudinal direction for each branch
k_s	translational stiffness in **z** direction provided by one branch
K	feedback controller gain
K_g	stiffness decomposed in orthogonal **x** or **y** direction for one flexure
K_s	translational stiffness in **z** direction provided by one guiding flexure
K_G	translational stiffness in **x** or **y** direction for one mass
l	length of one branch in a guiding flexure
M_*	mass, $* = U, L, F, B, i$
n	sample
r	radius of masses

Symbol	*Description*
s	*Laplace* operator
t	thickness of guiding flexures; time
u	steering signal
u_t	training input data
u_v	validation input data
v	auxiliary signal
x	axis; reference signal
y	axis; secondary path output
y_e	estimation output data
y_t	training output data
y_v	validation output data
z	axis

Greek symbols

Symbol	*Description*
κ_*	cutoff-frequency of $*$
ω_*	resonance frequency of $*$, $* = f, s, i, v$

Transfer functions

Symbol	*Description*
$C(s)$	feedback controller
$P(s)$	primary path transfer in continuous-time domain
$P(z)$	primary path transfer in discrete-time domain
$Q(z)$	high-pass filter
$S(s)$	secondary path transfer in continuous-time domain
$S(z)$	secondary path transfer in discrete-time domain
$W(z)$	feedforward control filter

Operators

Operator	*Description*
$(\cdot)^T$	transpose
$\mathrm{var}(\cdot)$	variance
$\lvert \cdot \rvert$	absolute value
$\hat{a}$	estimate of a
$\ddot{a}$	acceleration

Matrices

Operator	*Description*
$\mathbf{K}$	stiffness matrix
$\tilde{\mathbf{K}}$	normalized stiffness matrix
$\mathbf{M}$	mass matrix
$\mathbf{U}$	input vector
$\mathbf{X}$	displacement vector
$\ddot{\mathbf{X}}$	acceleration vector

Abbreviations/Acronyms

Abbreviation	*Description*
AVIC	Active Vibration Isolation Control
DOF	Degree-Of-Freedom
FIR	Finite Impulse Response
FxLMS	Filtered-x Least Mean Squares
ICs	Integrated Circuits
IIR	Infinite Impulse Response
IO	Input and Output
IPM	Ideal Physical Mode
LMS	Least Mean-Squares
LTI	Linear Time Invariant
MFxLMS	Modified Filtered-x LMS
PSD	Power Spectrum Density
SMI	Subspace Model Identification
VAF	Variance Accounts For

Contents

Acknowledgement

The past year is an amazing and unforgettable period in my study career. I jumped out of my five-year study at electrical engineering and devoted myself to a challenging but worthwhile project - a project that combines the theoretical design with its mechanical implementation at the Mechanical Automation Laboratory at the Department of Mechanical Engineering, University of Twente.

There are too many people I would like to thank. I'd like to give my sincere thanks to every member in the Mechanical Automation Group and Control Engineering Group, it is their efforts that gave a foreign student a warm home to stay and study. I would like to thank Prof. ir. H. Soemers for giving me the chance to do this challenging but interesting work and his brilliant ideas on designing the setup. My special gratitude goes to Dr. ir. J. van Dijk who shared so much time with me for questions and discussion, especially in the last two months of this project. Moreover, I would also like to thank my roommate, Jorg, who taught me various professional tools and helped me revise my report. My thoughts and thanks go also to L. Tiemersma, J. Eindhoven, G. Boersma and ir. G. W. van der Poel for their fruitful interaction over this year.

Last but not the least, I will never forget to say thanks to my parents, my grandmother, xiaojing, and my deceased grandpa, who steadily stood by me in my life despite the precious time that I was spending away from them.

Xiaohu Guo
Enschede, 27th June 2005

Chapter 1

Introduction

1.1 Project background

At the Mechanical Automation Laboratory, Department of Mechanical Engineering, University of Twente, one of the main research topics is Active Vibration Isolation Control (AVIC). One of the various projects in this topic is the PhD project *SMART MOUNT* in cooperation with The Technical University of Delft, the Netherlands and TNO-TPD. My master project is the first sub-project for *SMART MOUNT*, which aims at the design and realization of a one-dimensional setup for hard mounting active isolation purpose. Previous research at our laboratory dealt with the application of AVIC for reduction of machine structure borne sound. While in my project, AVIC is used to reduce the effects of the floor vibrations.

High precision machines

High precision equipment becomes more and more important in the modern technology. Especially in the field of integrated circuits (ICs) manufacturing, with the demand of decreasing size of chips, high precision is required. Therefore, vibration isolation of the sensitive tools such as lithography tools, optical microscopes, electron microscopes and e-beam systems becomes more and more an important issue. Take lithography machines for example, market demands for faster and more powerful IC chips are continually shrinking the line widths to the 0.25 micron level or even lower[11]. The vibration criteria for high precision machines which meet these smaller line width demands are more stringent than ever before.

In this project, we design and realize a one-dimensional demonstration setup to mimic the dynamics of the high-precision machines. This demonstration setup is to prove the viability of various hard mounting isolation approaches. Focus will be on the suppression of the suspension vibration modes of the mechanical structure.

Floor vibrations

There are three primary disturbance sources of vibrations for a high precision machine in a fab facility: floor vibrations, acoustic noise, and direct force disturbance. Among them, floor vibrations are often the main disturbance sources for high precision, vibration-sensitive equipment. It is usually the main environmental-borne disturbance in the $1 \backsim 100\,Hz$ frequency region as a mixture of stationary and non-stationary periodic and random noise with numerous sources.

The nature of floor vibrations makes it hard to measure and qualify them correctly. According to reference like [1], the stationary random components of floor vibrations are best characterized as the random noise and comply with the well-known VC-D curve ($6\,\mu m_{RMS}/s$, $8 \backsim 100\,Hz$), of which, in terts bands the floor velocity is often flat from $1\,Hz$ to $100\,Hz$. The periodic noise amplitude in floor vibrations is normally below $1\,\mu m_{RMS}/s$, mainly in the $20 \backsim 100\,Hz$ frequency range. And the non-stationary random floor vibrations could be a factor of 10 to extreme cases even a factor of 100 larger than follows from stationary noise analysis, amplitude rise to $50 \backsim 100\,\mu m/s$. Often the frequency of these vibrations coincides with building or floor dynamics. Like a wafer fab, a floor suspension at $2 \backsim 3\,Hz$ is expected.

In principle, measuring the VC-D level floor vibrations require a high sensitivity sensor with relative high price and big volume. In our project, a big mass body ($20\,kg$) will be used to reflect floor dynamics (a $3\,Hz$ floor suspension is designed), and an acceleration measured at this mass will be in the same frequency range ($1 \backsim 100\,Hz$) as the VC-D curve but with bigger amplitude to ensure that the signal measured with the selected sensor is above the sensor's noise level.

Why active hard mounting?

Vibration control can be split into passive and active means. The passive vibration control methods directly deal with the physical properties of a machine structure, like its stiffness, mass and damping ratio. The passive vibration control may boil down to a basic structural change, the use of other materials, or to the addition of a passive element. The idea of using passive methods is to mount the machine on a resiliently supported frame that acts like a low-pass filter, to filter out the vibrations from the floor. However, one disadvantage of using passive isolation means is its bad performance against the external or internal direct force disturbance.

In case the active vibration control does not rely on the machine structure, but uses sensors, actuators and a controller to generate an anti-force to compensate the disturbance. Then, it gives the possibility to achieve the same (or better) floor vibration isolation performance as using passive mount meanwhile persisting good isolation of the direct force disturbance by using the hard mounting technique. A comparison among three mainly used isolation

mounting techniques is in table 1.1. The active hard mounting technique which we are going to investigate in the *SMART MOUNT* project is better at isolation of the direct force disturbance than the other two soft mounting techniques. The essential question is whether the isolation performance of the active hard mounting for floor vibrations using novel control approaches can be as good as soft mount or better.

Table 1.1: *Comparison among different isolation means for direct force disturbance and floor vibrations (−: **bad;** 0: **medium;** +: **good**)*

	Direct force	Floor vibrations
Passive soft mount	−	**0**
Active soft mount	**0**	+
Active hard mount	+	?

Active isolation vibration control

As indicated in the previous section, active isolation vibration control does use sensors, actuators and a controller to generate an anti-force to compensate the disturbance. The basic idea of AVIC is that the vibration disturbances which need to be attenuated are measured on an appropriate place with sensors. Using these measured signals a steering signal is calculated using a suitable controller which should have the same amplitude but opposite phase as the disturbance signal. Then, assuming the system is linear, the anti-force generated by the actuators will cancel out the disturbance and finally the net output, which is the residual error, will be zero. The idea of AVIC is illustrated in figure 1.1.

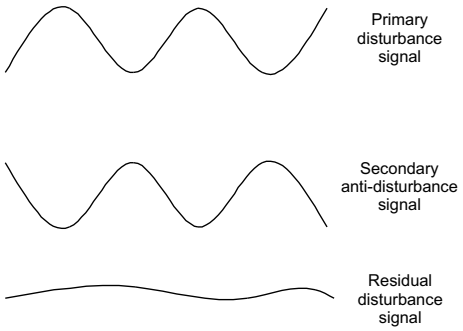

Figure 1.1: *Principle of superposition*

The types of AVIC systems can be sorted by the used controller. There are mainly two kinds of controllers: one is the feedforward controller, the other is the feedback controller. The feedforward controller which is normally solved in an adaptive manner can provide broadband noise attenuation. While the feedback controller provides artificial damping at the resonant peaks. Both of these two controllers have their advantages and disadvantages respectively. We will investigate these topics in this report.

Figure 1.2: *Model of a lens and its supporting frame used in a wafer stepper, provided by* Integrated Dynamics Engineering GmbH
(photo taken at the Mechanical Automation Laboratory, University of Twente)

1.2 Problem statement

We can divide the problem of my research into the following four parts:

- Figure 1.2 is the model of a lens and its supporting frame used in a wafer stepper. The primary goal of this project is to design a one-dimensional setup to mimic the suspension motions of the high precision tools, like shown in figure 1.2.
- With the model of the one-dimensional setup, we can simulate different types of controllers.
- Identification of the primary path and secondary path of the real one-dimensional setup is the third part in this project.
- The last step is to implement the classic fixed gain feedback control scheme on the one-dimensional setup.

1.3 Thesis outline

- Chapter 2 will concentrate on the design of the one-dimensional setup, starting with an analysis of the vibration modes, followed by determining the structure parameters and ends with considerations of mechanical implementations, special attention will be given to the one-dimensional motion realization.

- Chapter 3 will discuss three AVIC strategies: fixed gain feedback control, adaptive feedforward control using Modified Filtered-x LMS algorithms and one newly investigated control scheme: Induced Mode Control. Special attention will be given to the comparison of the classic feedback control and the induced mode control strategies. Simulation results will be given in this chapter.
- Chapter 4 will be concerned with the basic results obtained on the one-dimensional setup, including the primary path and secondary path identification using Subspace Model Identification technique, and the realtime experiments by implementing the classic fixed gain feedback control scheme.
- Chapter 5 gives a summary of the project and recommendations for further research.

Chapter 2

Design and analysis of the one-dimensional setup

2.1 Introduction

This chapter discusses the design and analysis of the one-dimensional setup. It starts with the development of the ideal physical model (IPM) of the one-dimensional setup in section 2.2, followed by a description of the relationship between vibration resonances and structure parameters in section 2.3. In section 2.4, we will examine the determined relationship by modal analysis. Finally, section 2.5 will concentrate on the mechanical implementations of the followings:

- Mass element design
- Stiffness realization
- One dimensional motion realization. That is: each mass in 3D space has 6 DOF motions. If only 1 DOF is desired for each mass body, then the motions in the other 5 DOF have to be constrained. We will address and emphasize the means we used to realize the one dimensional motion.

2.2 Structure breakdown

Figure 2.1 is a sketch of a positioning machine which is mounted on a passive pneumatic isolator, while Figure 2.2 depicts the piezo hard mounting technique, which is the active method we will investigate in this project. Regardless of the different mounting techniques, both figure 2.1 and figure 2.2 imply the vibration problem of the positioning machine: two suspension modes, one is the supporting mode caused by the compliance of the machine mount (passive or active), the other is the internal suspension caused by the compliance of the support between the upper and lower arm.

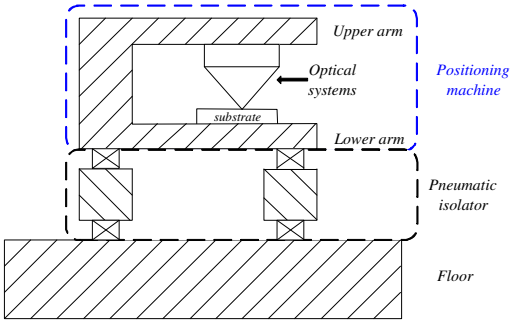

Figure 2.1: *Sketch of a high-precision positioning machine mounted on a passive pneumatic isolator*

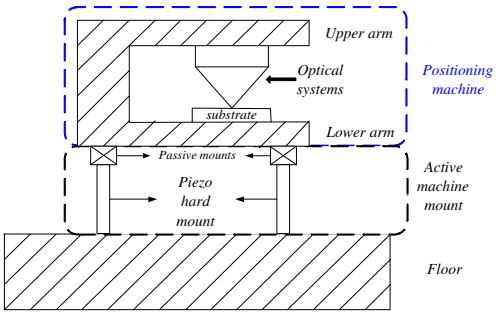

Figure 2.2: *Sketch of a high-precision positioning machine with active piezo mountings*

Figure 2.3[1] breaks down the piezo hard-mounted positioning machine shown in figure 2.2. M_U and M_L respectively represent the upper and lower working arm, while M_F represents the floor plate. k_3 is the stiffness of the piezo stack used as the active element, while k_2 is placed in series with the piezo in order to lower the supporting mode to desired frequency. The compliance of the floor is denoted as k_4, and k_1 reflects the compliance between the upper and lower arms. The complete ideal physical model (IPM) is shown in figure 2.3 (3). However, directly connecting the stiffness k_2 with a piezo stack causes difficulty for modelling when the piezo is used as a force supplier with certain stiffness. Therefore, a small virtual[2] mass M_B is inserted between k_2 and k_3 such that the force supplied from the piezo can be first transmitted to M_B instead of to the stiffness k_2. This action will facilitate the modelling process while it will not influence the dynamics in the interested frequency range by setting M_B to a very small value. The complete model with the virtual mass M_B is now shown in figure 2.4, with F_f and F_a respectively represent the disturbance force from shaker and anti-force from piezo-actuator. We will use this model for further conceptual design.

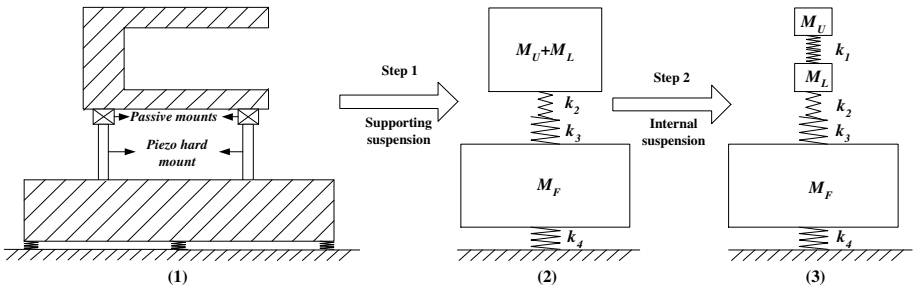

Figure 2.3: *Forming of ideal physical model*

[1]The model shown here is an undamped model.
[2]Virtual means that it only exists in conceptual design phase, but not in the real setup.

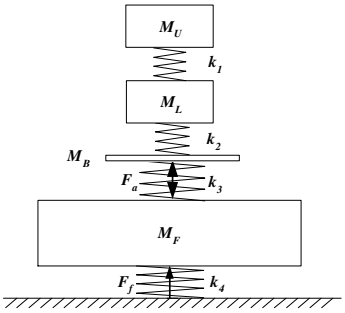

Figure 2.4: *Ideal physical model with the virtual mass M_B*

2.3 Mechatronic analysis of vibration modes

From a mechatronic design point of view, we can approximately decouple the model shown in figure 2.4 into several simple and standard systems. The decoupling process results in the four vibration modes depicted in figure 2.5. This method straightforwardly shows us the dynamics of the system, and by further analysis, we can determine the resonant frequency of each mode. However, this method can only provide an **approximate** solution, we will examine the results by modal analysis in the next section.

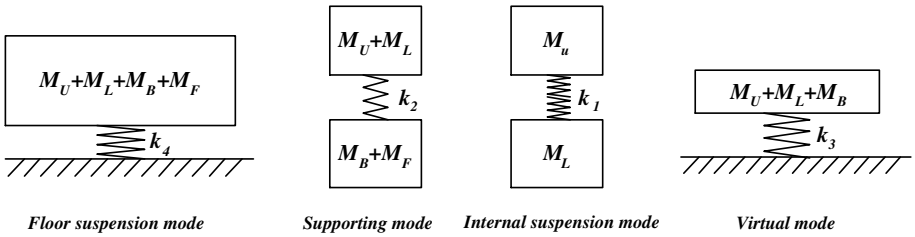

Figure 2.5: *Approximation of decoupled systems of the real* 1 *DOF setup*

From decoupled systems shown in figure 2.5, we can derive the four vibration modes symbolically as:

$$\omega_f \approx \sqrt{\frac{k_4}{M_U + M_L + M_B + M_F}} \tag{2.1}$$

$$\omega_s \approx \sqrt{k_2(\frac{1}{M_U + M_L} + \frac{1}{M_B + M_F})} \tag{2.2}$$

$$\omega_i \approx \sqrt{k_1(\frac{1}{M_U} + \frac{1}{M_L})} \tag{2.3}$$

$$\omega_v \approx \sqrt{\frac{k_3}{M_U + M_L + M_B}} \tag{2.4}$$

where, ω_f, ω_s, ω_i, ω_v respectively symbol the resonant frequency of the defined four vibration modes: floor suspension mode, supporting mode, internal suspension mode and virtual mode in the unit of radians per second.

Till now, we determined the relationship between the required resonant frequencies and the model parameters, the next step is to determine these four resonances. The supporting mode is expected at about $1\,Hz$ for the real high precision tools. Due to the reason that our wish is to research the viability of the active hard mounting technique, we choose the supporting mode with a frequency at $25\,Hz$. An internal mode of the lens system of a lithography tool is typically placed at $80\,Hz$. The floor suspension mode is set at $3\,Hz$ as we mentioned in chapter 1. While the virtual vibration is placed in a high and irrelevant frequency range. Table 2.1 lists the desired values for the resonances of the four vibration modes, in which f_f, f_s, f_i, f_v respectively are the resonant frequencies of the defined four

Table 2.1: *Resonance of vibration modes of the setup*

Floor vibration mode: f_f	$3\,Hz$
Supporting mode: f_s	$25\,Hz$
Internal suspension mode: f_i	$80\,Hz$
Virtual vibration mode: f_v	$> 1000\,Hz$

vibration modes. By substituting these four desired resonances into equations 2.1, 2.2, 2.3 and 2.4, we can find various sets of data for M_U, M_L, M_B, M_F and k_1, k_2, k_4[3]. Finally, considering the practical situation, like setup volume, available space in the laboratory, we determine the model parameters as listed in table 2.2.

Table 2.2: *Model parameters*

M_U $[kg]$	M_L $[kg]$	M_B $[kg]$	M_F $[kg]$	k_1 $[N/m]$	k_2 $[N/m]$	k_3 $[N/m]$	k_4 $[N/m]$
2.5	2.5	0.1	20	1.2×10^5	3×10^5	6×10^6	7000

However, because the relationship shown in equations 2.1, 2.2, 2.3 and 2.4 are only approximate solutions. In order to ensure the data that we listed in table 2.2 are accurate enough to make the setup have the desired four resonances, we will verify them using modal analysis.

[3] k_3 is the equivalent stiffness of piezo stack and is prefixed as $6 \times 10^6 N/m$.

2.4 Resonances check by modal analysis

It is handy and straightforward to describe a system by writing out its differential equations. However, for a multi-degree-of-freedom system like the one we are dealing, analyzing the system by its differential equations means complex and heavy calculations. On the other hand, modal analysis has the advantage of the symmetric algebraic eigenvalue problem, which allows the power of mathematics to be used in solving vibration problems and allows the use of mathematical software packages for analyzing systems with an arbitrary number of degrees of freedom. Additionally, the natural frequencies which we are interested in can be generalized by connecting the undamped-vibration problem to mathematics of the algebraic eigenvalue problem. In this section, we will examine the data listed in table 2.2 to ensure that it corresponds to the desired resonances in table 2.1.

To apply modal analysis, we first write out the system's differential equations using Newton's Law:

$$\begin{cases} M_U\ddot{x_U} &= -k_1(x_U - x_L) \\ M_L\ddot{x_L} &= k_1(x_U - x_L) - k_2(x_L - x_B) \\ M_B\ddot{x_B} &= k_2(x_L - x_B) - k_3(x_B - x_F) + F_a \\ M_F\ddot{x_F} &= k_3(x_B - x_F) - k_4x_F + F_f - F_a \end{cases} \tag{2.5}$$

where $\ddot{x}$ represents the acceleration profile. We can easily rewrite the equation 2.5 in a state space representation:

$$\begin{pmatrix} M_U & 0 & 0 & 0 \\ 0 & M_L & 0 & 0 \\ 0 & 0 & M_B & 0 \\ 0 & 0 & 0 & M_F \end{pmatrix} \times \begin{pmatrix} \ddot{x_U} \\ \ddot{x_L} \\ \ddot{x_B} \\ \ddot{x_F} \end{pmatrix} = \begin{pmatrix} -k_1 & k_1 & 0 & 0 \\ k_1 & -(k_1+k_2) & k_2 & 0 \\ 0 & k_2 & -(k_2+k_3) & k_3 \\ 0 & 0 & k_3 & -(k_3+k_4) \end{pmatrix} \times \begin{pmatrix} x_U \\ x_L \\ x_B \\ x_F \end{pmatrix} + \begin{pmatrix} 0 & 0 & 0 & 1 \\ 0 & 0 & 1 & -1 \end{pmatrix}^T \times \begin{pmatrix} F_f \\ F_a \end{pmatrix} \tag{2.6}$$

Furthermore, by defining the following matrix in symbolic form:

$$\mathbf{X} = \begin{pmatrix} x_U \\ x_L \\ x_B \\ x_F \end{pmatrix}; \qquad \ddot{\mathbf{X}} = \begin{pmatrix} \ddot{x_U} \\ \ddot{x_L} \\ \ddot{x_B} \\ \ddot{x_F} \end{pmatrix}; \qquad \mathbf{U} = \begin{pmatrix} F_f \\ F_a \end{pmatrix};$$

where $\mathbf{X}$ is called displacement vector, by differentiating twice, we get acceleration vector $\ddot{\mathbf{X}}$. Due to the fact that the system's dynamics does not rely on the external excitation, we can ignore the input force F_f and F_a from equation 2.5, and define other matrices:

$$\mathbf{M} = \begin{pmatrix} M_U & 0 & 0 & 0 \\ 0 & M_L & 0 & 0 \\ 0 & 0 & M_B & 0 \\ 0 & 0 & 0 & M_F \end{pmatrix}; \qquad \mathbf{K} = \begin{pmatrix} -k_1 & k_1 & 0 & 0 \\ k_1 & -(k_1+k_2) & k_2 & 0 \\ 0 & k_2 & -(k_2+k_3) & k_3 \\ 0 & 0 & k_3 & -(k_3+k_4) \end{pmatrix};$$

where $\mathbf{M}$ is called the mass matrix and $\mathbf{K}$ is the stiffness matrix. Finally, we obtain a simplified state space representation (in form of $\ddot{x} = Ax + Bu$):

$$\mathbf{M}\ddot{\mathbf{X}} = \mathbf{K}\mathbf{X} \tag{2.7}$$

Note that the physical nature of both the mass and stiffness matrix is symmetric, hence, preserving this symmetry is a natural approach for solving the vibration problem by modal analysis[4]. Since $\mathbf{M}$ is symmetric and positive definite, it may be factored into two terms:

$$\mathbf{M} = \mathbf{L}\mathbf{L}^T \tag{2.8}$$

where $\mathbf{L}$ is a special lower triangular matrix. Then, the next step is to calculate the normalized stiffness matrix by following equation:

$$\tilde{\mathbf{K}} = \mathbf{L}^{-1/2}\mathbf{K}\mathbf{L}^{-1/2} \tag{2.9}$$

Finally, we can convert the resonant frequencies of the vibration problem into solving the symmetric eigenvalue problem of $\tilde{\mathbf{K}}$. By substituting the data in table 2.2 into the matrices $\mathbf{M}$ and $\mathbf{K}$, we calculate[5] the corresponding resonances at: $2.6\,Hz$, $26\,Hz$, $78\,Hz$ and $1250\,Hz$, which are very close to the desired resonances. Now, we can come to the conclusion that the data we listed in table 2.2 are precise enough to obtain the desired four resonances.

2.5 Mechanical structure consideration

In the previous section, we determined the model parameters of the one-dimensional setup. Our attention in this section will be drawn to the mechanical implementations of these parameters. We will respectively consider the mass element design, the stiffness implementation of k_1, k_2 and the one dimensional motion realization in this section.

2.5.1 Mass element design

Only M_U, M_L and M_F will appear in the real one-dimensional setup, while the virtual mass M_B only has its function in conceptual design step. Because our goal is to investigate the suspension vibration modes of the one-dimensional setup, the bending deformation of each mass body should happen only at high frequency ($> 300\,Hz$). Due to this consideration, the three masses are designed in disc shape with data listed in table 2.3.

All the mass bodies are made from steel, with *Young's modulus* $E = 200 \times 10^9\,Nm^{-2}$. Besides the above consideration, the determination of the height and radius of these mass bodies also involves the realization of the 1 dimensional movement. We will elaborate on this topic later.

[4]For the reader who is interested in modal analysis method, I refer to [3].
[5]Calculation is done by MATLAB.

Table 2.3: *Design data of three masses*

	M_U	M_L	M_F
Weight $[kg]$	2.5	2.5	20
Height d $[mm]$	28	28	112.5
Radius r $[mm]$	60	60	85
Material	Steel	Steel	Steel

2.5.2 Implementation of the stiffness of k_1 and k_2

The stiffnesses k_1 and k_2 shown in figure 2.4 are implemented by the translational stiffness in **z** direction provided by the flexure as shown in figure 2.6. The flexure has three identical branches, with its thickness t, width h and length l.

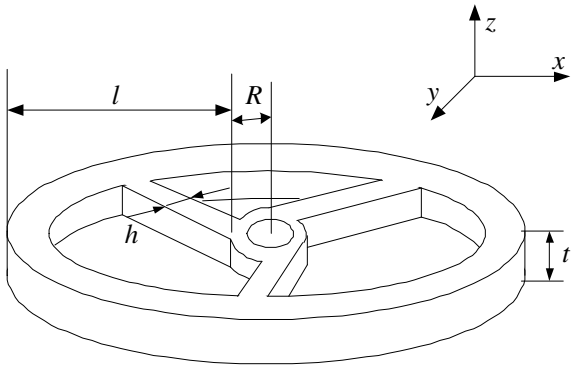

Figure 2.6: *Flexure*

When the outer ring of the flexure is fixed to the fixed world, each branch can be treated as a beam which is *Fixed at One End, Free but Guided at the Other*, then it will provide stiffness k_s in **z** direction as shown in figure 2.7. The translational stiffness in **z** direction provided by each branch can be calculated:

$$k_s = 12\frac{EI}{l^3} \tag{2.10}$$

where I is the second moment of inertia, and in our case:

$$I = \frac{ht^3}{12} \tag{2.11}$$

Substitute equation 2.11 into equation 2.10, we have:

$$k_s = \frac{Eht^3}{l^3} \tag{2.12}$$

The translational motion in **z** direction for a flexure is now shown in figure 2.8. The total stiffness in **z** direction provided by one flexure is contributed by the three branches as:

$$K_s = 3 \times k_s = 3\frac{Eht^3}{l^3} \tag{2.13}$$

where K_s represents the translational stiffness provided by one flexure in the **z** direction.

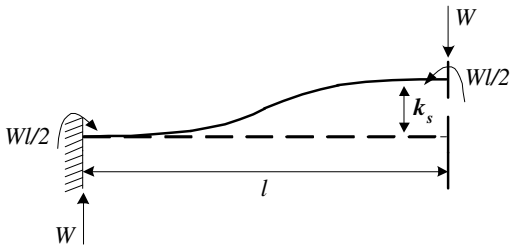

Figure 2.7: *Translational stiffness k_s in* **z** *direction provided by one branch*

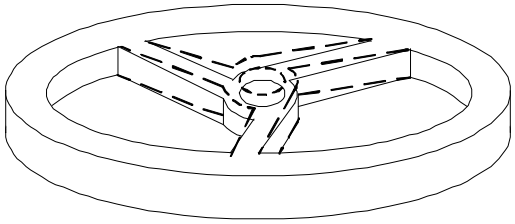

Figure 2.8: *Translational stiffness K_s in* **z** *direction provided by one flexure*

Equation 2.13 describes the relationship between the stiffness of k_1, k_2 and the structure parameters of the flexure. As listed in the table 2.1, k_1 is $3 \times 10^5\, N/m$ and k_2 is $1.2 \times 10^5\, N/m$. Table 2.4 lists the structure parameters of flexures to provide these two stiffnesses as their translational stiffnesses in **z** direction.

Table 2.4: *Design data of the flexures for k_1 and k_2*

	k_1	k_2
Stiffness [N/m]	3×10^5	1.2×10^5
Length l $[mm]$	40	40
Thickness t $[mm]$	2	2
Width h $[mm]$	4	1.6
Material	Steel	Steel

2.5.3 1 dimensional guiding function realization

One important issue in the mechanical design step is to realize the 1 DOF guiding function for each mass body, that is: how to constrain the 5 DOF motions and keep only 1 DOF motion for every of the three mass bodies. Because we use the same means for this purpose for each mass, we will start with explaining the 1 DOF motion realization for a single mass body. Then, we will go to the overall solution for the whole setup.

Figure 2.9 explains the means to constrain the 5 DOF motions and allow only 1 DOF motion for one mass body. The mass body is disc shaped as we designed it in the previous section with radius r and thickness d. Three identical springs having a $120\,^\circ$ angle with each other are placed at both the top and bottom sides of the mass. The effect of these six springs is to constrain the mass' in-plane motions: translation motion in **x** and **y** direction and the rotational motion around **z** axis, as well as the mass' rotational motion around **x**, **y** axis[6]. In other words, the resonances caused by the translational or rotational modes

[6]Figure 2.11 on page 19 specifically displays this motion.

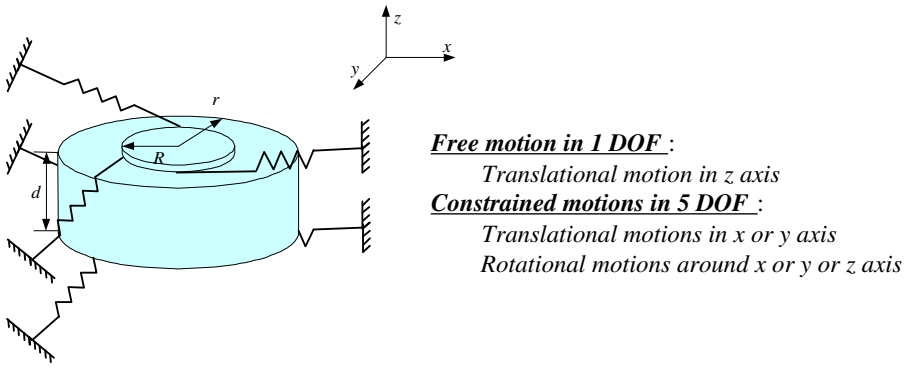

Figure 2.9: *The implementation of a 1 DOF guider for a single mass body*

in any of the 5 unwanted DOF should be well constrained by the corresponding stiffness provided by the guiding springs. The criterion to judge whether the motions in the 5 unwanted DOF are well constrained is: These resonances should occur at least at a frequency 4 times higher than the highest frequency that we are interested in. Because the highest resonance in our interest is the $80\,Hz$ internal mode, we have:

$$f_{critertion} \geq 4 \times 80 = 320\,Hz \tag{2.14}$$

The three springs at either the top or bottom of the mass body are integrated into one guiding flexure with its shape shown in figure 2.6. Each spring is functioned by one branch in the guiding flexure. In following subsections, we will derive the equations to calculate the resonances caused by the motions in the 5 unwanted DOF.

Translational mode in x and y direction

As the cross-section of each branch of the guiding flexure shown in figure 2.6 is rectangular, we can define the stiffness of each branch in its longitudinal direction as:

$$k_g = \frac{EA}{l} \tag{2.15}$$

where k_g represents the stiffness of each branch in its longitudinal direction, E is the *Young's modulus*, l and A are the length and cross-section of the branch. $A = h \times t$, where h and t are the width and the thickness of the branch. Because we are interested in the stiffness in **x** and **y** direction, we decompose the stiffness of the three branches in their longitudinal direction into **x** and **y** direction, then for small displacements, we have the stiffness provided by one flexure in **x** or **y** direction as:

$$K_g = 1.5 \times k_g = 1.5\frac{EA}{l} \tag{2.16}$$

where K_g represents the stiffness provided by one flexure in orthogonal **x** or **y** direction. Because we use two flexures on both the top and bottom sides for each mass body, the stiffness in orthogonal **x** or **y** direction for each mass should be 2 times K_g:

$$K_G = 2 \times K_g = 3\frac{EA}{l} \tag{2.17}$$

The resonance caused by the translational modes in **x** or **y** direction is now constrained by the translational stiffness K_G provided by the guiding flexures for each mass:

$$f_1 = \frac{1}{2\pi}\sqrt{\frac{K_G}{m}} = \frac{1}{2\pi}\sqrt{\frac{3EA}{lm}} \tag{2.18}$$

where m is the weight of the mass body.

Torsional mode - rotational motion around z axis

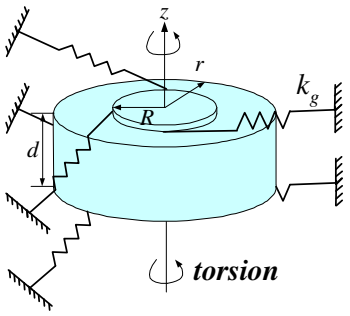

Figure 2.10: *Suspension motion caused by the torsional mode*

Besides the translational motions in **x** or **y** direction, another in-plane unwanted motion is caused by the rotational mode around **z** axis, which is the so called torsional mode. Figure 2.10 is the indication of torsional motion as mentioned. The corresponding torsional stiffness for each mass body provided by one branch in one flexure is:

$$c_{torsion} = k_g \times R^2 = \frac{EA}{l} \times R^2 \tag{2.19}$$

where k_g is the stiffness for each branch in its longitudinal direction, while R is indicated in figure 2.10. Then, for one flexure, the total torsional stiffness is:

$$C_{torsion} = 3 \times c_{torsion} = 3 \times \frac{EA}{l} \times R^2 \tag{2.20}$$

Because each mass body is fixed by two flexures as shown in figure 2.9, the total torsional stiffness for each mass body is 2 times of $C_{torsion}$:

$$C_{TO} = 2 \times C_{torsion} = 6 \times \frac{EA}{l} \times R^2 \tag{2.21}$$

The resonance caused by the torsional mode for each mass is now constrained by the torsional stiffness provided by the guiding flexures as:

$$f_2 = \frac{1}{2\pi}\sqrt{\frac{C_{TO}}{I_j}} = \frac{1}{2\pi}\sqrt{\frac{6EAR^2}{lI_j}} \tag{2.22}$$

where I_j is the polar moment of inertia [4] of the mass body around the **z** axis:

$$I_j = \frac{1}{2}mr^2 \tag{2.23}$$

Finally, by substituting equation 2.23 into equation 2.22, we have:

$$f_2 = \frac{1}{2\pi}\sqrt{\frac{12EhtR^2}{mlr^2}} \tag{2.24}$$

Tilting mode - rotational motion around x or y axis

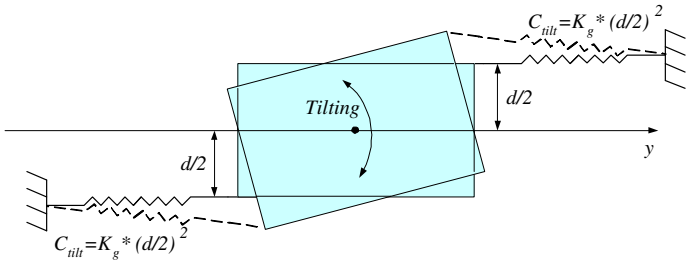

Figure 2.11: *Suspension motion caused by the tilting mode*

The last kind of the unwanted motions is the rotational motion around **x** or **y** axis, which is the so called tilting motion as indicated in figure 2.11. The tilting stiffness provided by each flexure in either **x** or **y** direction is:

$$C_{tilt} \approx K_g \times (\frac{d}{2})^2 = \frac{3}{8}\frac{EAd^2}{l} \tag{2.25}$$

where C_{tilt} is the tilting stiffness for each mass body provided by one flexure, and d is the thickness of the mass body. Because C_{tilt} is the tilting stiffness decomposed in **x** or **y** axis, K_g is used instead of k_g in equation 2.25. As there are two flexures for each mass, the total tilting stiffness for each mass body is:

$$C_{TI} = 2 \times C_{tilt} = \frac{3}{4}\frac{EA}{l} \times d^2 \tag{2.26}$$

The resonance caused by the tilting motion is now constrained by the tilting stiffness provided by the guiding flexures:

$$f_3 = \frac{1}{2\pi}\sqrt{\frac{C_{TI}}{I_g}} = \frac{1}{2\pi}\sqrt{\frac{3EAd^2}{4lI_g}} \tag{2.27}$$

where I_g is the polar moment of inertia of the mass body around **x** or **y** axis:

$$I_g = \frac{1}{4}mr^2 \tag{2.28}$$

Finally, the tilting resonance turns out to be:

$$f_3 = \frac{1}{2\pi}\sqrt{\frac{3Ehtd^2}{lmr^2}} \tag{2.29}$$

where d is the thickness of the mass body, and h, t, l as defined in figure 2.6.

The unconstrained $1-DOF$ motion- translational motion in z direction

The stiffness provided by the guiding flexures in **z** direction for each mass is also interesting because it should be low enough to provide a relatively free motion in this direction. The translational stiffness in **z** direction provided by one flexure was already formalized in equation 2.13.

In the next section, we will first determine the structure parameters of the guiding flexures, and then calculate the resonances for the 5 unwanted motions to see whether they all meet the design criterion: $f > f_{criterion}$.

2.5.4 Overall structure

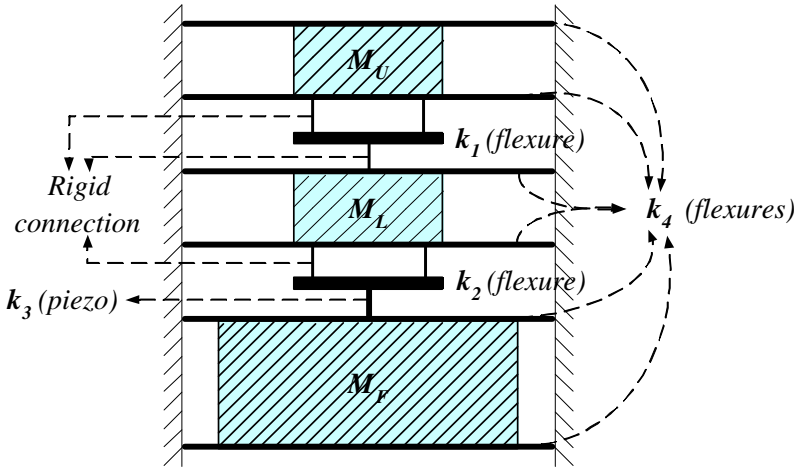

Figure 2.12: *The realization of k_4 by six identical guiding flexures*

As we discussed in the previous section, there are three masses in total, and each of these three masses will have two identical guiding flexures to perform the guiding function. Therefore, totally six identical flexures are used for these three masses. The overall structure is now available in figure 2.12. The stiffness k_4 is now performed by the total stiffness in the **z** direction of the six identical flexures, so we have:

$$k_4 = 6 \times K_s = 18 \times \frac{Eht^3}{l^3} = 7000\,N/m \tag{2.30}$$

By the relation described in equation 2.30, we determine the parameters for the guiding flexures in table 2.5, where the *Young's modulus* value of the used material is $200 \times 10^9\,Nm^{-2}$.

With the determined structure parameters of the flexures, we are now able to examine the guiding function of the flexures for each mass. Table 2.6 lists the stiffness in the 5 unwanted DOF provided by the guiding flexures as we discussed in the previous section. From table 2.6, all the resonances caused by the unwanted modes are well constrained by

Table 2.5: *Parameter settings for the guiding flexures*

	Length l [mm]	*Thickness t [mm]*	*Width h [mm]*	*Material*
Guiding flexure	100	0.5	16	*Steel*

the corresponding stiffness and meet the design criterion: $f > f_{criterion}$ except the resonance caused by the torsional mode of the mass M_F. However, a small torsional rotation in the $\mathbf{x}-\mathbf{y}$ plane hardly gives any influence for the translational motion in the $\mathbf{z}$ direction.

Table 2.6: *Guiding stiffness for the 5 unwanted DOF and the corresponding resonances for each mass*

		M_U	M_L	M_F
Translational stiffness [N/m]	$K_G = 3\frac{EA}{l}$	5×10^7	5×10^7	5×10^7
Translational resonance [Hz]	$f_1 = \frac{1}{2\pi}\sqrt{\frac{3EA}{lm}}$	800	800	300
Torsional stiffness [Nm]	$C_{TO} = 6 \times \frac{EA}{l} \times R^2$	1.3×10^5	1.3×10^5	1.3×10^5
Torsional resonance [Hz]	$f_2 = \frac{1}{2\pi}\sqrt{\frac{12EhtR^2}{mlr^2}}$	855	855	215
Tilting stiffness [Nm]	$C_{TI} = \frac{3}{4}\frac{EA}{l} \times d^2$	9382	9382	1.5×10^5
Tilting resonance [Hz]	$f_3 = \frac{1}{2\pi}\sqrt{\frac{3EAd^2}{4lI_g}}$	325	325	326

One step further, as we mentioned before, the guiding flexures should provide relative free translational motion in $\mathbf{z}$ direction. In other words, the compliance of the guiding flexures in $\mathbf{z}$ direction should not influence the stiffness of k_1 and k_2, so as to change the prefixed supporting and internal resonances. Take k_2 for example, the compliance of the flexures actually changes the supporting resonance by putting a stiffness of $4 \times K_s$ in parallel with k_2, with K_s the translational stiffness in $\mathbf{z}$ direction provided by one guiding flexure. Figure 2.13 depicts the guiding flexures' influence on k_2. However, because $k_2 = 1.2 \times 10^5\, N/m$, while $4 \times K_s \approx 4500\, N/m$, the guiding flexures hardly have any influence on k_2. After all, we can draw the conclusion that the expected guiding function is well realized by the designed guiding flexures.

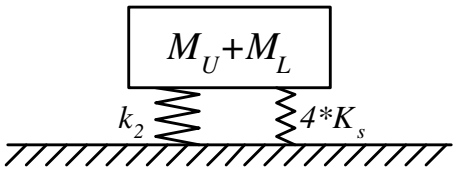

Figure 2.13: *The influence of the guiding flexures on the supporting suspension mode*

2.6 The one-dimensional setup

The side view and front view of the one-dimensional setup that we designed are now captured in figure 2.14 and figure 2.15. The set-up is implemented horizontally instead of its vertical schematic that we used for analysis. The flexures now also play the role of compensating the gravity and keeping the center of each mass in the right position. The working part of the setup is encompassed in a tube which functions as the fixed world. Because of the transparency of the tube (made of plexi-glas), we are able to observe the working part of the setup. There are three accelerometers on those three masses. From the front view of the setup, the exciter for the primary path is displayed, with three threads connecting to the big round black ring which rigidly connects to the fixed frame.

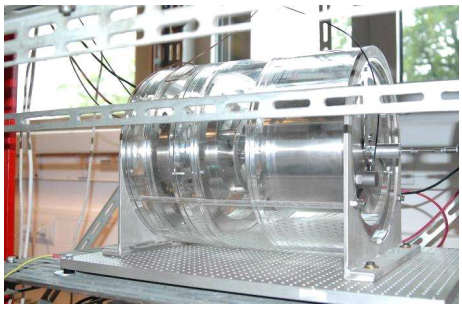

Figure 2.14: *The side view of the one-dimensional setup*

Figure 2.15: *The front view of the one-dimensional setup*

2.7 Summary

In this chapter, we started with forming the ideal physical model of a hard mounted positioning machine. Then, by introducing a virtual mass M_B, we found the equations to calculate the four desired vibration resonances with mechatronic analysis means. These equations **approximately** defined the relation between the desired four resonances and the model parameters. Later on, we selected a proper set of parameters which complies with equations 2.1 $\backsim$ 2.4 and examined them with modal analysis tool. Validation results proved that, with the selected parameters, the setup model gave us the desired four resonances.

In the second half of this chapter, we considered the mechanical implementations of these structure parameters and drew attention to the means to realize the one dimensional motion. The three masses were designed such that their bending deformation modes are well above the frequencies in interest. The stiffnesses k_1 and k_2 were realized by the flexures by their translational stiffness in **z** direction. Special attention was given to constraining the motions in the 5 unwanted directions for each mass. Two identical flexures were designed at both ends of every disc-shaped mass. Final examination results showed that the proper designed flexures achieved to constrain the resonances caused by the vibration modes in the 5 unwanted DOF at high enough frequencies outside of interest. Meanwhile, the six flexures also provided the desired stiffness for floor suspension by their total translational stiffness in **z** direction. All the analysis helped us reach the conclusion that the guiding function is well performed by the designed guiding flexures.

Chapter 3

Controller design

In the previous chapter, we designed and analyzed the one-dimensional setup. In this chapter, we will pay attention to the control issues of the one-dimensional setup. As we described in figure 1.1 in Chapter 1, the basic principle of active vibration isolation control is to generate a proper secondary anti-disturbance signal, such that it cancels the disturbance from the primary path and finally the residual error measured at the error sensor is zero. Various ways to calculate a proper anti-signal from the secondary path are advocated [5], [6], and in here three different control strategies are discussed:

- The adaptive feedforward control using the modified Fxlms algorithm;
- The classic fixed gain feedback control;
- The induced mode feedback control.

Later on, because of the similarity of the classic feedback and induced mode feedback control algorithms, special attention will be given to the comparison of these two control strategies.

3.1 Definition of primary path and secondary path

Let's first recall the setup model we established in chapter 2, figure 3.1 is the setup model with virtual mass M_B as well as disturbance force F_f from the exciter, anti-force F_a from the piezo actuator and three accelerometers[1] for each mass. For further discussion in this chapter, we define the primary and secondary path transfer functions in continuous-time domain as:

For the *Primary Path* transfer function, the input is defined to be the acceleration of M_F, and the output is the acceleration of M_L when only F_f is applied to the system:

$$P(s) = \frac{\ddot{x}_L}{\ddot{x}_F}(s)$$

[1]The positions of the sensors in figure 3.1 does not correspond to the positions of the accelerometers in the real setup.

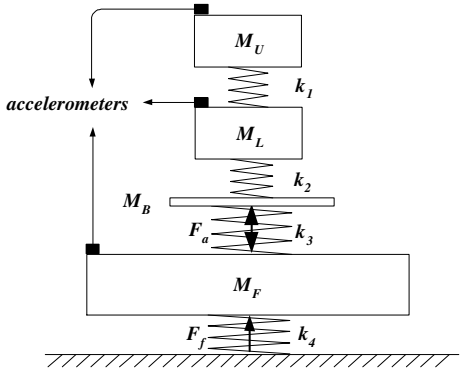

Figure 3.1: *Setup model with accelerometers*

Since only the acceleration instead of the excitation force of the real ground is measurable in the real situation, we define the acceleration of M_F instead of F_f as the input of the primary path.

For the *Secondary Path* transfer function, the input is defined to be the force from the piezo-actuator and the output is the acceleration of M_L when only the piezo-actuator supplies power to the system:

$$S(s) = \frac{\ddot{x}_L}{F_a}(s)$$

The equivalent discrete-time domain transfer functions of $P(s)$ and $S(s)$ are $P(z)$ and $S(z)$.

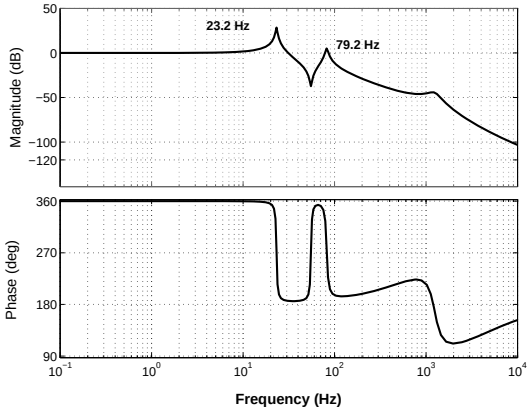

Figure 3.2: *Bode plot of the primary path* $P(s) = \frac{\ddot{x}_L}{\ddot{x}_F}(s)$

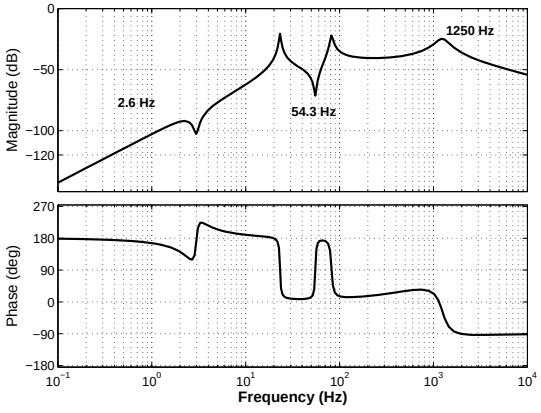

Figure 3.3: *Bode plot of the secondary path* $S(s) = \frac{\ddot{x}_L}{F_a}(s)$

With these definitions, by substituting the determined parameters into the setup model as shown in figure 3.1, we can build up the setup's `SIMULINK` model. Figures 3.2 and 3.3 depict the Bode plots of the above defined primary and secondary path transfer functions. There is about 2% damping installed at the supporting and the internal suspension modes,

and more damping for the floor suspension mode and the virtual mode to reflect the structural damping in the real one-dimensional setup. From the primary path Bode plot, we detect three resonances respectively at $23.2\,Hz$, $79\,Hz$ and $1250\,Hz$. The first two are precisely what we expected as the supporting and internal suspension modes, while the last resonance at $1250\,Hz$ is obviously at a high and irrelevant frequency and is caused by the virtual mass M_B. In the other Bode plot in figure 3.3, as the secondary path is defined from force to acceleration, we also detect the floor suspension resonance at $2.6\,Hz$. Furthermore, one important property of the secondary path transfer function $S(s)$ is that there are no right half plane zeros in S(s). As a result, $S(s)$ is a minimum-phase system and its inverse transfer is also stable. Figure 3.4 is the pole-zero map of $S(s)$[2].

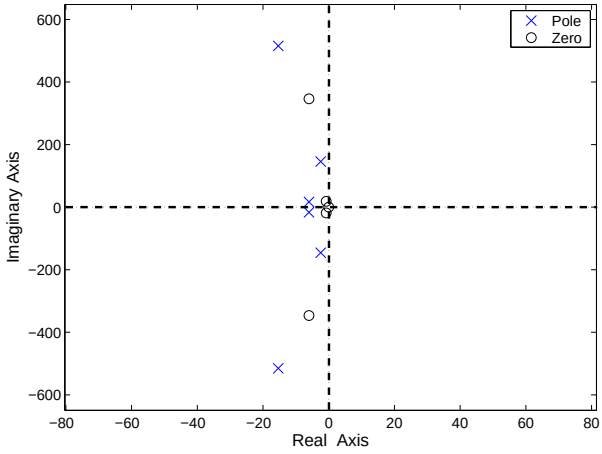

Figure 3.4: *Pole-Zero map of the secondary path transfer function $S(s)$*

3.2 Adaptive feedforward control using the modified filtered-x LMS algorithm

Before we come to the adaptive feedforward solution for vibration problems, we first briefly introduce the basis of adaptive filter theory. Figure 3.5 shows the basic structure of the adaptive filter using the LMS algorithms [5]. The adaptive filter can be thought as consisting of two parts: the actual filter $W(z)$ and the adaptive algorithm that updates the filter coefficients using the reference signal $x(n)$ and the error signal $e(n)$. The update law for LMS algorithm is based on the method of steepest decent algorithm [6]. Both finite impulse response (FIR) and infinite impulse response (IIR) structures can be implemented for the filter $W(z)$. The FIR structure only incorporates zeros which makes it unconditionally stable, while the IIR structure has poles which can move outside the unit circle during the adaptation process, causing instability. Most adaptive filters therefore make use of a FIR filter structure and this structure is used for active vibration isolation control purposes here.

[2]Several poles and zeros whose real parts are smaller than -100 are not captured in this figure.

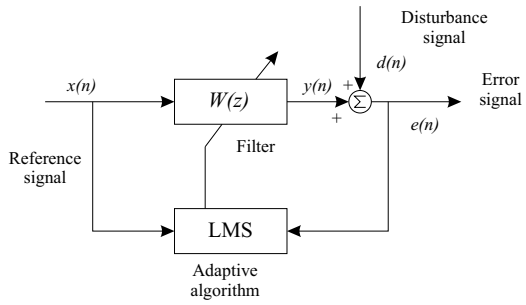

Figure 3.5: *Block diagram of an adaptive filter*

Figure 3.6 shows the basic idea of the feedforword active vibration control problem, where $P(z)$ and $S(z)$ respectively represents the discrete primary and secondary transfer functions. A disturbance signal $x(n)$ results in $d(n)$ from the primary path $P(z)$ at the error sensor. The disturbance $d(n)$ will be reduced by generating an appropriate control filter output $u(n)$, and sending it through the secondary transfer path $S(z)$, resulting in the anti-disturbance signal $y(n)$. In order to perform feedforward control, we assume that the signal $x(n)$ is measurable as a reference signal to the control filter $W(z)$.

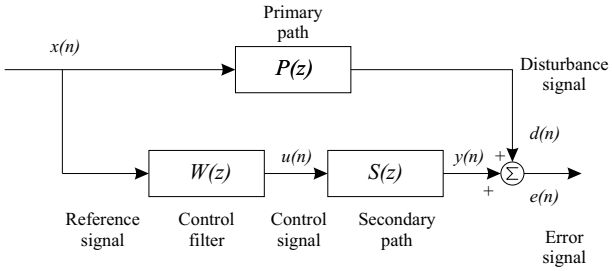

Figure 3.6: *Basic block diagram of a feedforward AVIC system*

Then, the question comes to how to design a proper feedforward controller $W(z)$ such that it can make the secondary path to generate a proper anti-signal. One widely used method is solving the problem in an adaptive manner, and this method can be directly conducted from figure 3.6, in which the controller $W(z)$'s structure is constructed as FIR filter and coefficients are determined by LMS algorithm. Compared with figure 3.5, the introduction of the secondary path transfer $S(z)$ requires a modification of the standard implementation of the LMS adaptive filter [6]. The most well developed and suitable solution for modification is the Filtered-x LMS algorithm, which is to place an identical filter $\hat{S}(z)$ in the reference signal path to the filter coefficients update of the LMS algorithm[13], with $\hat{S}(z)$ the estimation of the true secondary path transfer $S(z)$.

However, due to the minimum-phase-zero property of $S(z)$ in our specific case, which results in a stable inverse of $S(z)$, hereby, we advocate a simpler solution [9]: Modified Filtered-x LMS algorithm (MFxLMS). The structure of MFxLMS is shown in figure 3.7. From this figure, we can see that in the MFxLMS algorithm, an inverse filter $\hat{S}^{-1}(z)$ is

placed in the secondary path, resulting in a cancellation of the secondary path effect on the LMS algorithm.

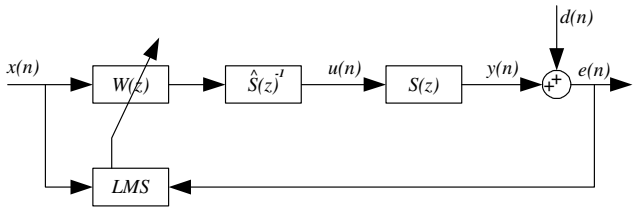

Figure 3.7: *Ideal MFxLMS implementation*

Although the inverse of $S(z)$ is stable, due to the low gain of $S(z)$ at low frequencies as shown in figure 3.3, a very high gain at the low-frequent part of $\hat{S}^{-1}(z)$ can be expected. Then the low-frequent high gain in $\hat{S}^{-1}(z)$ will lead to a large steering signal $u(n)$ which finally causes the saturation for the piezo actuator. To avoid this circumstance, a high-pass filter can be installed to filter out the low-frequent high output of $\hat{S}^{-1}(z)$. The structure of MFxLMS with the high-pass filter $Q(z)$ is now available in figure 3.8. The criterion for the selection of the order and cutoff frequency of $Q(z)$ is to lower the low-frequent components of the steering signal $u(n)$ into the piezo's linear working region.

The MFxLMS algorithm in figure 3.8 provides faster adaptation and less adaptation taps than normal Filtered-x LMS algorithms, where taps are the number of coefficients used in the FIR filter. It eliminates the effect of secondary path and results in a standard adaptive filtering problem as shown in figure 3.5. However, we sacrifice the low frequent control effect by introducing a high pass filter to avoid the piezo's saturation. Besides, as it is only developed to accommodate situations where the secondary path is *minimum phase*, the usage of this kind of inverse filter is limited.

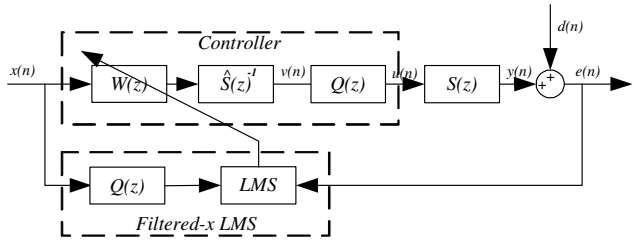

Figure 3.8: *Structure of the MFxLMS algorithm with the high-pass filter $Q(z)$*

Broadband disturbance noise rejection by the MFxLMS algorithm

Due to time restriction, I did not implement the MFxLMS algorithm on the one-dimensional setup. Following are the simulation results of implementing the MFxLMS strategy on the

one-dimensional setup model. The simulation was done for broadband ($1 \backsim 1000\,Hz$) disturbance rejection by feeding a random noise signal into $x(n)$ which results a disturbance signal $d(n)$ at the error sensor as shown in figure 3.10 (first 25 seconds snapshot).

We construct $\hat{S}(z)$ by inserting an additional zero at high frequency ($200Hz$) to $S(z)$ to add some modelling error. We chose the high-pass filter $Q(z)$ to be a 2^{nd} order high pass filter with its cutoff frequency at $2\,Hz$.

By inserting $P(z)$, $S(z)$, $\hat{S}(z)$ and $Q(z)$ into the MFxLMS schematic, setting the adaptation taps for LMS algorithm to 1000[3], where taps are the number of coefficients used in the FIR filter, finally we got the controlled residual error signal $e(n)$ as shown in last 25 seconds snapshot in figure 3.10. Figure 3.9 depicts the adaptation process of the last 5 coefficients out of 1000 taps.

Because of the insertion of $Q(z)$ and the secondary path modelling error by the additional zero, as well as the limitation of the adaptation taps we used, we are not able to obtain perfect cancellation. However, we obtained about $30\,dB$ reduction between the disturbance signal $d(n)$ and the residual error $e(n)$. Figure 3.11 compares the spectrum power density of the signals $d(n)$ and $e(n)$, from which we can easily observe the noise attenuation effect in the frequency range from $2\,Hz$ to $200\,Hz$ (about $60\,dB$ and $40\,dB$ noise attenuation respectively at $25\,Hz$ and $80\,Hz$ resonances in this simulation example).

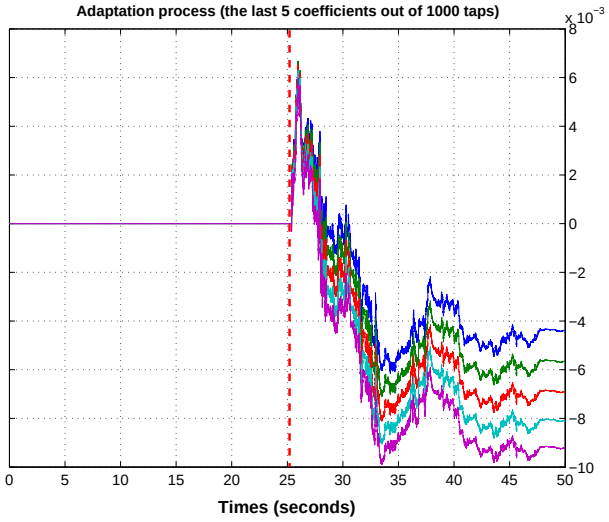

Figure 3.9: *Adaptation process of the last* 5 *coefficients out of* 1000 *taps*

[3]This is an ideal simulation setting due to the computation complexity for the realtime processor.

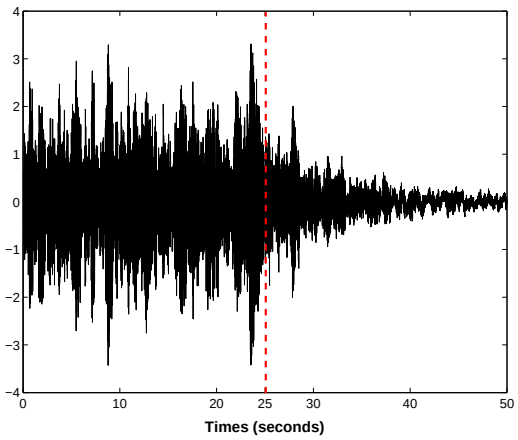

Figure 3.10: *Time domain broadband disturbance rejection with controller turned on at t=25 s, L=1000*

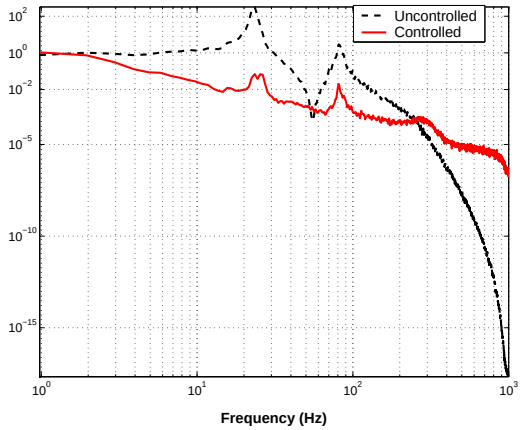

Figure 3.11: *Power spectrum density of signals $d(n)$ and $e(n)$*

3.3 Classic fixed gain feedback control

In the previous section, we introduced the general adaptive feedforward algorithm for vibration problems and discussed the modified FxLMS algorithm for the one-dimensional setup. In this section we will expand our efforts on the conventional control strategy – fixed gain feedback control. Unlike feedforward control, which attempts to gain noise reduction in a broad frequency band, feedback control can only have its control effect in a certain frequency range mainly due to stability constraints. However, the advantage of using feedback against the adaptive feedforward is that, adaptive feedforward is from a computational viewpoint which is more complex than fixed gain feedback control, while fixed gain feedback is expected to have about the same performance in case of broadband disturbance.

In this section, based on the defined primary and secondary paths, we will introduce a *+PI+* controller which is based on the idea of velocity feedback for the acceleration measurement case.

3.3.1 Design of the *+PI+* feedback controller

Figure 3.12 gives the general schematic of a fixed gain feedback control strategy for vibration problems. A controller $C(s)$ is designed such that the error signal e can track a zero reference r, finally resulting a zero error e in the control bandwidth range. In our case, the output error signal is the acceleration of M_L. As a result, a PI controller is suitable to build up a virtual damper between the masses M_L and M_F.

The design of $C(s)$ involves both gaining damping performance at the $25\,Hz$ and $80\,Hz$ resonances and ensuring stability of the closed loop system. The stability problem in vibra-

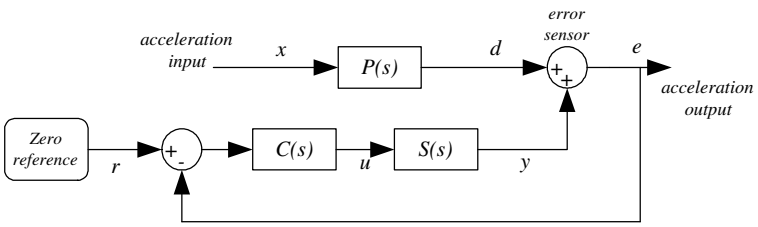

Figure 3.12: *General structure of a classic fixed gain feedback control for vibration problems*

tion control is more complex than that of motion control, because more than one crossover will appear due to the multi-resonance characteristic of vibration problem. Therefore, we should pay attention to each of these crossovers. The $+PI+$ controller should comply with the following requirements:

- Damp the $25\,Hz$ and $80\,Hz$ resonances[4]
- Control action ends before $300\,Hz$ to ensure stability, because un-modelled resonances are present at high frequencies like the resonances caused by the tilting or torsional modes.

The design procedure for $C(s)$ is listed step by step below. The frequency unit for the open-loop design is radians per second.

Step 1: Design of a double tame-integrator $DL(s)$ with poles set at low frequencies, which pulls the phase at low frequency down from $+180\,^{\circ}$.

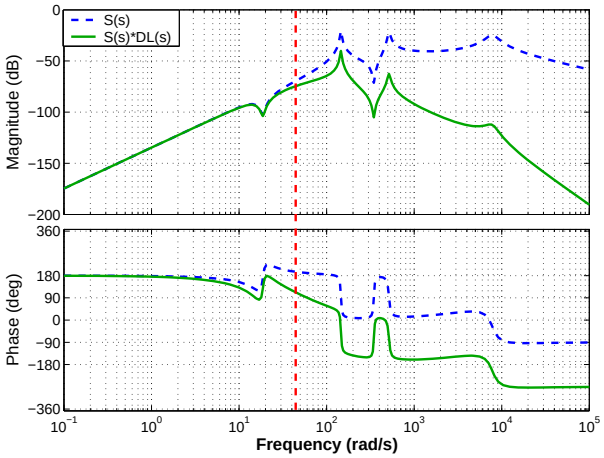

Figure 3.13: *Bode plots of* $S(s)$ *and* $S(s) \times DL(s)$

$$DL(s) = \frac{\kappa_{DL}^2}{s^2 + 2\kappa_{DL}s + \kappa_{DL}^2} \tag{3.1}$$

[4]We do not specify the noise attenuation level because the structural damping in the real setup is unknown.

where κ_{DL} is the designed cut-off frequency for $DL(s)$, and should be placed before the minimum crossover frequency for $C(s)$. Figure 3.13 depicts both the Bode plots of $S(s)$ and $S(s) \times DL(s)$, with $\kappa_{DL} = 50\,rad/s$. From figure 3.13, we find the double tame-integrator generates more phase margin in the frequency range before the first resonance $25\,Hz$ ($157\,rad/s$). However, the double tame-integrator also reduces the phase margin after $25\,Hz$.

Step 2: Calculate the gain K of $C(s)$ to meet the desired open loop crossover. Figure 3.14 depicts the Bode plots of $DL(s) \times S(s)$ and $K \times DL(s) \times S(s)$, for the desired open loop crossover at $\kappa_d = 60\,rad/s$. From figure 3.14 we can observe that the first crossover of $K \times DL(s) \times S(s)$ is now at about $60\,rad/s$, and has about 90 degrees phase margin. However, the phase of the second crossover at about $110\,rad/s$ almost reaches to -180 degrees.

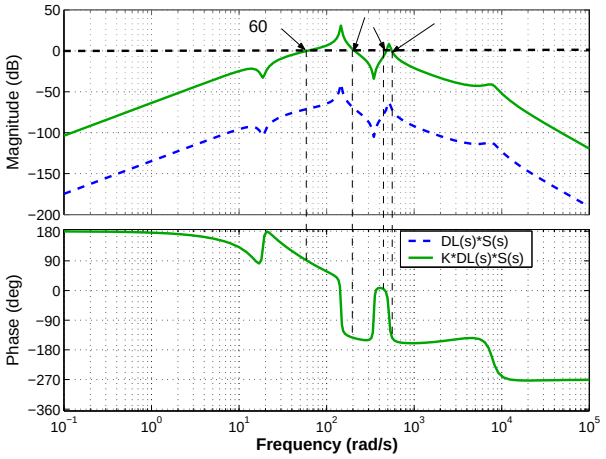

Figure 3.14: *Bode plots of* $DL(s) \times S(s)$ *and* $K \times DL(s) \times S(s)$, $K \approx 80dB$

Step 3: In order to provide enough phase margin for the second and fourth crossovers, we can add one zero before the first resonance at $25\,Hz$ ($157\,rad/s$) such that it will install +90 degrees phase for each crossover except the minimum one.

$$ZH(s) = \frac{1}{\kappa_{ZH}}s + 1 \tag{3.2}$$

where κ_{ZH} is the expected frequency where to stop the *double integrating* action and start the *single integrating* action. Figure 3.15 shows the Bode plots of $K \times DL(s) \times S(s)$ and $K \times DL(s) \times ZH(s) \times S(s)$, with $\kappa_{ZH} = 80\,rad/s$. From figure 3.15, we have three observations: the first one is that the use of $ZH(s)$ has little influence on the phase of the first crossover, the second one is that it now provides enough phase margin for the second and fourth crossovers. However, it also introduces a fifth crossover which might become a candidate for stability problems.

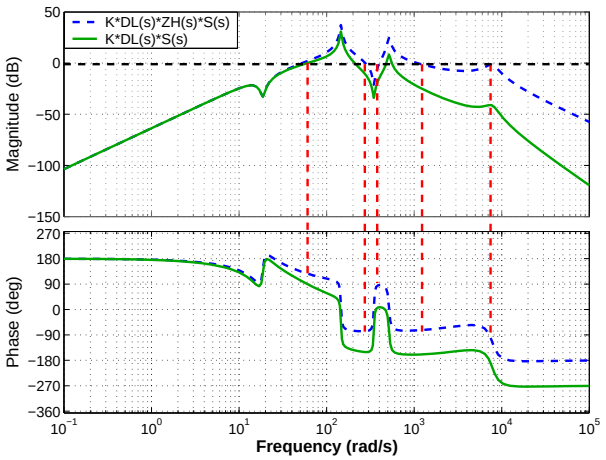

Figure 3.15: *Bode plots of* $K \times DL(s) \times ZH(s) \times S(s)$ *and* $K \times DL(s) \times S(s)$

Now, we finished the design of the PI controller, and the next step is to explain the design of the two $+$ actions.

Step 4: A high pass filter with cutoff frequency κ_{HP} $(< \kappa_{DL})$ is the first $+$ which means there will be hardly any or no control action before the cut-off frequency κ_{HP}. The main reason to do so is that the piezo-actuator is hardly to apply big enough anti-force to compensate the primary disturbance at low frequencies because the secondary path transfer function has very low gain at low frequencies where the primary path transfer function has $0\,dB$ transmissibility.

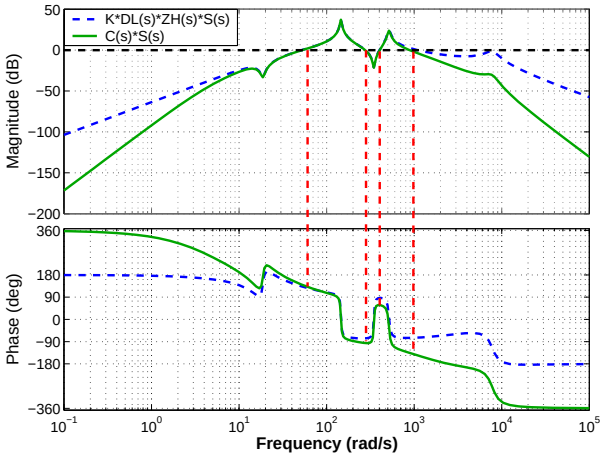

Figure 3.16: *Bode plots of* $K \times DL(s) \times ZH(s) \times S(s)$ *and* $K \times DL(s) \times ZH(s) \times F_{HL}(s) \times S(s)$

Meanwhile, a low pass filter with cutoff frequency κ_{LP} between $80\,Hz$ $(500\,rad/s)$ and $300\,Hz$ $(1900\,rad/s)$ is designed as the second $+$ in order to provide more roll off

to install more safety against resonance frequency uncertainty, e.g. the fifth crossover.

$$F_{HL}(s) = F_L(s)F_H(s) = \frac{\kappa_{LP}^2}{s^2 + 2\kappa_{LP}s + \kappa_{LP}^2} \times \frac{s^2}{s^2 + 2\kappa_{HP}s + \kappa_{HP}^2} \tag{3.3}$$

Figure 3.16 depicts the Bode plots of $K \times DL(s) \times ZH(s) \times S(s)$ and $K \times DL(s) \times ZH(s) \times F_{HL}(s) \times S(s)$ with $\kappa_{LP} = 1500\,rad/s$ $(= 238\,Hz)$ and $\kappa_{HP} = 10\,rad/s$ $(= 1.6\,Hz)$. It is clear that we have achieved additional roll off before κ_{HP} and after κ_{LP}. However, the selection of κ_{LP} and κ_{HP} should be done very carefully. As shown in figure 3.16, the introduction of $F_L(s)$ pulls down the phase at the fourth crossover close to $-180\,^\circ$. Meanwhile, $F_H(s)$ lifts up the phase at the first crossover close to $+180\,^\circ$. To avoid stability problem, κ_{HP} and κ_d, as well as κ_{LP} and the fourth crossover should be designed as far as possible.

Finally, the controller is:

$$C(s) = K \times DL(s) \times ZH(s) \times F_{HL}(s) \tag{3.4}$$

The Bode plot of the open loop was displayed as the green solid curve in figure 3.16. The control bandwidth, which is the frequency at which the open loop system gain is above $0\,dB$, is from about $10\,Hz$ to $170\,Hz$. Figure 3.17 gives the closed loop results of implementing the designed $C(s)$ into the schematic shown in figure 3.12. The results shown in figure 3.17 correspond to our theory: the feedback controller installs *artificial damping* for the interesting resonances[5] and has no control action in other frequencies.

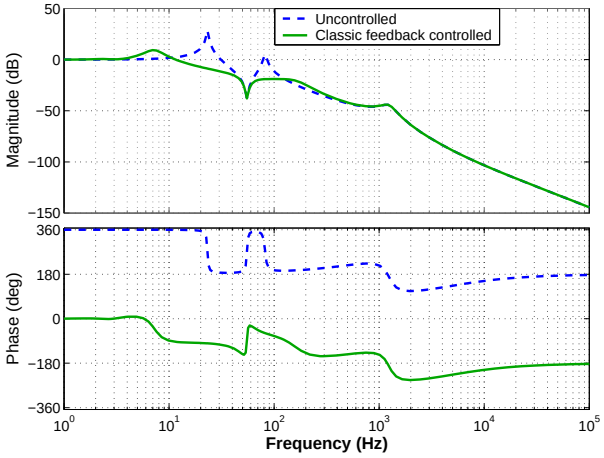

Figure 3.17: *Bode plots of the closed loop system $\frac{e}{x}(s)$ using the fixed gain feedback controller*

3.4 Induced mode control

Besides the discussed conventional feedback control and the adaptive feedforward control strategies, recently a novel controller for vibration problems has arose in the Mechanical

[5]One interesting phenomena is that the closed loop curve pumps up in the neighborhood frequency before $25Hz$ and after $80Hz$.

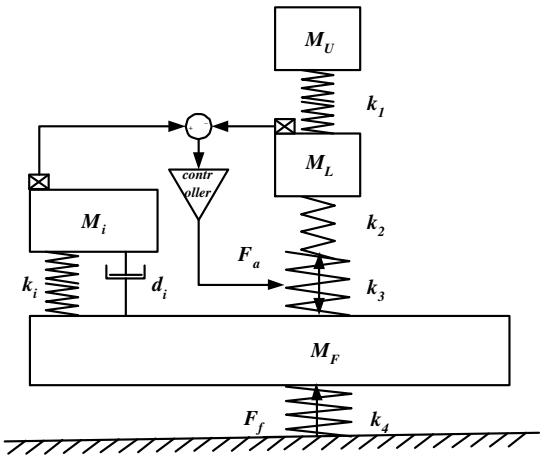

Figure 3.18: *Physical interpretation of induced mode control*

Automation Laboratory, which is called Induced Mode Control. Hereby, we investigate this novel approach because of its potential to provide better low-frequent control compared to the classic fixed gain feedback approach.

The idea of induced mode control is directly derived from its physical meaning as shown in figure 3.18. In figure 3.18, there is an ideal passively isolated system composed of mass M_i, spring k_i and damper d_i, with its resonance called the induced mode. The physical interpretation is that we want M_L in the one-dimensional setup to have the same isolation performance as M_i. From a control viewpoint, we subtract the measured acceleration $\ddot{x}_L$ with a reference r, but instead of the zero reference that we used in the conventional feedback in the previous section, we use the acceleration measured at M_i. The ideal passive isolated system (M_i, k_i, d_i) is realized in software and has no physical counterpart.

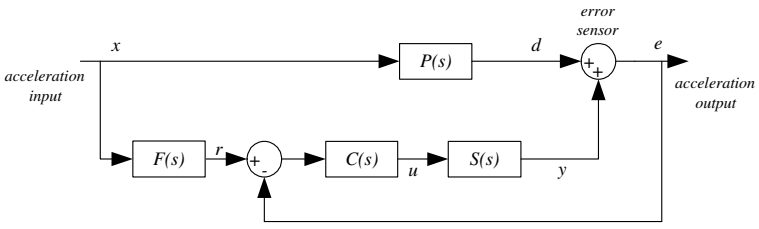

Figure 3.19: *Schematic of induced mode control*

Based on the idea of the classic fixed gain feedback control strategy that we discussed in the previous section, we introduce the schematic of the induced mode control as shown in figure 3.19. In figure 3.19, the ideal passively isolated system is modelled as a pre-filter $F(s)$ with input the acceleration of M_F, and output the acceleration of M_i: $\ddot{x}_i$.

The design of an induced mode controller involves the design of the controller $C(s)$ as well as the pre-filter $F(s)$. The design of $C(s)$ adapts the result from the previous section

except the high-pass filter $F_H(s)$. In induced mode control, the function of $F_H(s)$ is taken by the pre-filter $F(s)$. As a result, the controller is:

$$C(s) = K \times DL(s) \times ZH(s) \times F_L(s) \tag{3.5}$$

Then, the problem comes to how to realize the ideal passively isolated system as a pre-filter $F(s)$. First of all, it is necessary to know that the design of $F(s)$ greatly depends on the definition of the primary path transfer function $P(s)$. For example, as $P(s)$ in the beginning of this chapter was defined from $\ddot{x}_F$ to $\ddot{x}_L$, then $F(s)$ should be defined as from $\ddot{x}_F$ to $\ddot{x}_i$. However, in the case if the $P(s)$ is defined as from the force F_f to $\ddot{x}_L$, then $F(s)$ should be defined as from F_f to $\ddot{x}_i$[6], that is:

$$F(s) = \frac{\ddot{x}_i}{F_f}(s) = \frac{\ddot{x}_i}{\ddot{x}_F}(s) \times \frac{\ddot{x}_F}{F_f}(s)$$

Let's inherit the definition $P(s) = \frac{\ddot{x}_i}{\ddot{x}_F}(s)$. With the induced mode (M_i, k_i, d_i) shown in figure 3.18, by setting $k_i = 90\,N/m$, $d_i = 20\,kg/s$, $M_i = 1\,kg$, we can obtain an ideal passive isolation system with a cutoff frequency at $\omega_i = 10 rad/s$ ($\omega_i = 1.5\,Hz$) with its Bode plot shown in figure 3.20. From its Bode plot, the induced mode approximately has a 1^{st} order low-pass characteristic. The Bode plot of the closed loop system using the induced mode control strategy is now available in figure 3.21.

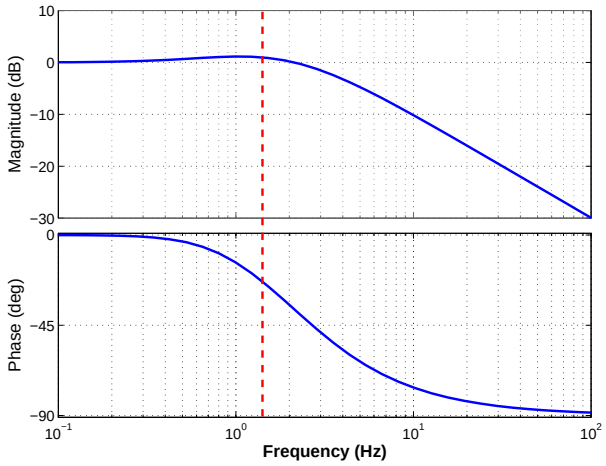

Figure 3.20: *Bode plot of the pre-filter $F(s)$, $k_i = 90\,N/m$, $d_i = 20\,kg/s$, $M_i = 1\,kg$*

3.5 Comparison of classic feedback and induced mode control

From figure 3.17 and figure 3.21, we can hardly find any difference between the closed loop results from the conventional feedback control and the induced mode control. These

[6]This is the primary path definition for the realtime experiments in the next chapter.

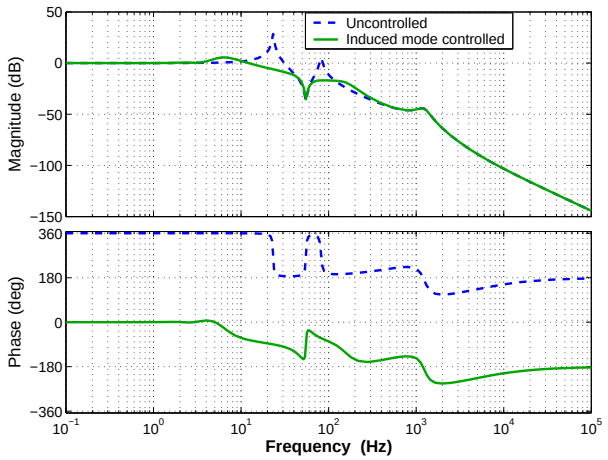

Figure 3.21: *Bode plots of the closed loop system* $\frac{e}{x}(s)$ *using the induced mode control*

two strategies started from different points but finally converged to the same effect. From control point of view, the induced mode control moves the high-pass filter $F_H(s)$ in the controller $C(s)$ in classic feedback control to a pre-filter $F(s)$. Table 3.1 compares the differences between these two control strategies.

Table 3.1: *Comparison of the classic feedback control and the induced mode control* ($\kappa_{HP} = \omega_i$)

	Classic feedback control	**Induced mode control**
Description	Zero reference for the servo-loop and a second order high-pass filter $F_H(s)$ with cut-off frequency at κ_{HP} is constructed in the controller.	Non-zero reference for the servo and a 1^{st} order low-pass filter $F(s)$ with cutoff frequency ω_i is constructed as a pre-filter.
Low freq. $< \omega_i, \kappa_{HP}$	*Weak* control	*Perfect* non-control
Low-frequency robustness	$F_H(s)$ is included in the servo-loop and influences the phase of the low-frequent open-loop crossover, so as to the stability of the closed loop system.	$F(s)$ is a pre-filter and is not included in the servo-loop. Therefore, it has no influence on the closed loop stability.

3.6 Comparison of the passive and active isolation means for the one-dimensional setup

Figure 3.22 compares the noise reduction by using the passive and active isolation means on the one-dimensional setup model. The passive isolation starts e.g. from $1.5\,Hz$, while to make it comparable, the induced mode feedback controller starts from $1\,Hz$. The ideal passive isolation cornered at $1.5\,Hz$ provides more attenuation than feedback control except in the frequency range near the $1.5\,Hz$ peak. The passive isolation achieves a $-40\,dB$ slope attenuation from its corner frequency $1.5\,Hz$, while the feedback active isolation only achieves roughly a $-20\,dB$ slope attenuation in its controlled range.

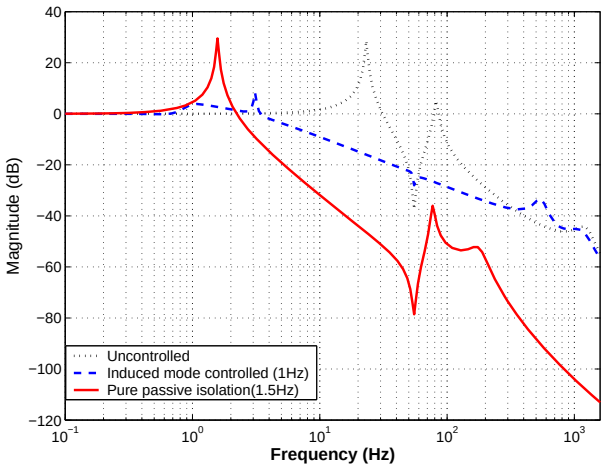

Figure 3.22: *Simulation results of the passive isolation with* $1.5\,Hz$ *corner frequency and the active isolation by the induced mode feedback control with* $\omega_i = 1\,Hz$

However, the following topics in further researches indicate the potential of using active vibration isolation means:

- To combine the fixed gain feedback control strategy (classic or induced mode) with adaptive feedforard control. Then, on one hand, the adaptive feedforward algorithm helps to gain a broadband noise reduction to make it comparable to the passive isolation, on the other hand, the feedback controller installs *artificial damping* at the resonance peaks to speed up the convergence of the adaptive feedforward algorithm.

- To build up a sky-hook damper in the ideal passively isolated system in the induced mode control scheme. Then, instead of a $-20\,dB$ slope of noise attenuation, the sky-kook damper might help to achieve a $-40\,dB$ noise attenuation.

3.7 Summary

In this chapter, we provided three different control strategies: adaptive feedforward control using the modified Filtered-x LMS algorithm; classic fixed gain feedback control and

induced mode feedback control. The adaptive feedforward solution can provide noise attenuation in a broadband frequency range, while the other two feedback solutions installs artificial damping at the frequencies where resonances occur.

MFxLMS is derived for the one-dimensional setup model because the secondary path $S(z)$ of the one-dimensional setup has no unstable zeros and its inverse transfer exists and is stable. The simulation showed that by using the MFxLMS strategy, we obtained about $30\,dB$ noise reduction between the disturbance signal $d(n)$ and the residual error $e(n)$ in a broadband frequency range. However, the performance of MFxLMS greatly depends on the high pass filter $Q(z)$, the quality of the secondary path estimation $\hat{S}(z)$ and the number of adaptation coefficients used in FIR filter.

In the later sections in this chapter, we introduced two feedback control algorithms. Classic feedback is directly derived from a common feedback control problem, while induced mode control is derived from the physical interpretation of an ideal passive isolation system. We listed the steps for designing these two controllers and also analyzed the advantages and disadvantages of these two feedback control strategies.

Finally, we compared the passive isolation result with the active means using the induced mode control on the one-dimensional setup model. The comparison showed the advantage of using the passive isolation means when dealing with floor vibrations as we indicated in chapter 1. But the potential of using active isolation by combining the fixed gain feedback (classic or induced mode) with the adaptive feedforward strategy or building a sky-hook damper in the ideal passively isolated system for induced mode control was seen from the comparison.

Chapter 4

Primary and secondary paths identification and realtime control results

In chapter 2 and 3, we discussed issues about the design and control of the one-dimensional setup. In this chapter, the primary and secondary path transfer functions $P(z)$ and $S(z)$ from the real one-dimensional setup are identified by the Subspace Model Identification tool. Then the classic feedback control algorithm that we discussed in the previous chapter will be implemented on the one-dimensional setup. The induced mode control and the modified Filtered-x LMS algorithms have not been tested on the setup due to the limited available time.

The definitions of the primary path $P(s)$ and secondary path $S(s)$ were given in section 3.1. However, for reason of simplicity, in the following identification and control, the definition of the primary path in the discrete-time domain will be changed to[1]:

$$P(z) = \frac{\ddot{x}_L}{F_f}(z) \tag{4.1}$$

While the secondary path transfer function definition remains the same as in section 3.1:

$$S(z) = \frac{\ddot{x}_L}{F_a}(z) \tag{4.2}$$

4.1 Primary and secondary path identification

4.1.1 Preliminary considerations

Before we start to identify the primary and secondary path transfer functions, it is necessary to know how much force is approximately needed to excite the primary path to generate an audible but still piezo-compensatable noise [10] . The type of piezo stack

[1]The change of the primary path definition will not have any influence on the control issues.

Table 4.1: *Specifications of the selected piezo-actuator*

Type	max. stroke $[\mu m]$	length $[mm]$	stiffness $[N/m]$
Pst 150/5/400 VS10	50	46	12×10^6

that would be used in the one-dimensional setup is **Pst 150/5/...VS10**, with its general specifications [12] listed in table 4.1. Since the piezo stack is placed between M_L and M_F, the displacement difference between M_F and M_L reflects the elongation of the piezo stack. The rule to keep the piezo working in the safe range is to limit its elongation to half of its maximum stroke. The maximum stroke of the selected piezo is $50\,\mu m$ as listed in table 4.1. Therefore $0 \backsim 25\,\mu m$ is the piezo's safe elongation range. The following steps will estimate the required force of F_f to generate a few microns ($< 25\,\mu m$) displacement difference between M_L and M_F.

Let's first recall the setup model in figure 2.4, then the following two approximate transfer functions can be calculated directly:

$$\frac{x_F}{F_f}(s) \approx \frac{1}{(M_U + M_L + M_F)s^2 + k_4} \tag{4.3}$$

$$\frac{x_L}{F_f}(s) = \frac{x_F}{F_f}(s) \cdot \frac{x_L}{x_F}(s) \approx \frac{1}{(M_U + M_L + M_F)s^2 + k_4} \cdot \frac{k_{23}}{(M_U + M_L)s^2 + k_{23}} \tag{4.4}$$

where k_{23} is the equivalent stiffness putting k_2 and k_3 in series, $k_{23} \approx k_2 = 1.2 \times 10^5\, N/m$. Then, by subtracting equation 4.4 from equation 4.3, we have the transfer function from the force F_f to the displacement difference between M_L and M_F, and its frequency response $H(j\omega)$ can be written as:

$$H(j\omega) = \frac{x_F(j\omega)}{F_f(j\omega)} - \frac{x_L(j\omega)}{F_f(j\omega)} \tag{4.5}$$

Therefore, we have:

$$|x_F(j\omega) - x_L(j\omega)| = |H(j\omega)||F_f(j\omega)| \tag{4.6}$$

The same calculations can also be done for the secondary path. Then, we also have:

$$|x_F(j\omega) - x_L(j\omega)| = |H'(j\omega)||F_a(j\omega)| \tag{4.7}$$

Figure 4.1 depicts the frequency response of both $H(j\omega)$ and $H'(j\omega)$. Two important conclusions can be drawn:

- The excitation force F_f for the primary path should be selected such that it causes a maximum displacement difference between M_L and M_F less than half of the piezo's max. stroke, that is $25\mu m$. We can see that the blue dashed curve in figure 4.1

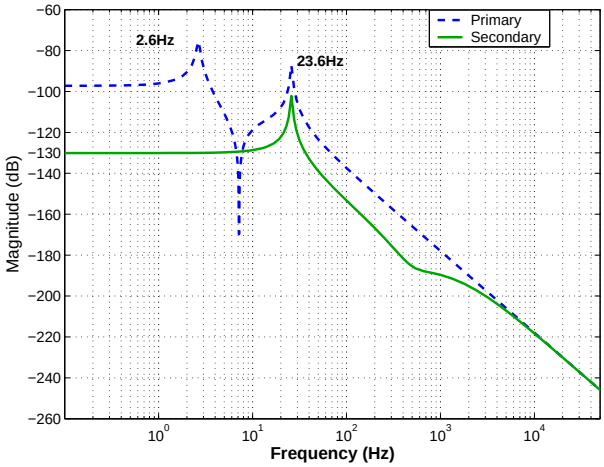

Figure 4.1: *Frequency response of $H(j\omega)$ (dashed) and $H'(j\omega)$ (solid)*

has a higher gain at low frequencies ($< 5\,Hz$) than at other frequencies. The gain in $0\,Hz \backsim 5\,Hz$ is about $-100\,dB = 10^{-5}$, which means $1\,N$ excitation force will generate $10\,\mu m$ elongation of the piezo, which is within the piezo's safe elongation range. However, we also observe that the peaks at $2.6\,Hz$ and $23.6\,Hz$ have an even higher gain than $-100\,dB$. Therefore, to accommodate the peaks at $2.6\,Hz$ and $23.6\,Hz$, the excitation F_f is determined to be a force with amplitude $0.3N$ in the frequency range $1 \backsim 1000\,Hz$.

- On the other hand, it is also interesting to see that from $1\,Hz$ to $1000\,Hz$, the gain of the green solid curve, which is the transmissibility of $H'(j\omega)$, is lower than the blue dashed one. That indicates that a large force is required from the piezo-actuator to compensate a relatively small disturbance excitation from the primary path. For example, at $f = 1\,Hz$, if a disturbance $F_f = 0.3\,N$ is applied to the primary path, which generates about $3\,\mu m$ displacement difference between M_L and M_F, while for the piezo, about $10\,N$ force is required to compensate for it.

4.1.2 Identification of the primary and secondary paths

The setup models are identified using **S**ubspace **M**odel **I**dentification (SMI) techniques[7], [8]. To use the SMI techniques, first of all, we have to construct proper input & output (IO) pairs of the primary and secondary paths. The primary path $P(z)$ and secondary path $S(z)$ are estimated separately with a sampling frequency $f_s = 2\,kHz$ during 20 seconds. So totally, $20 \times 2000 = 40000$ data samples are obtained for each. The input data for both primary and secondary path is a binary number generated by the *PRBS* toolbox[2]. The amplitude of the input is selected such that the primary and secondary paths will separately generate an equal amplitude output ($\ddot{x}_L$). Figures 4.2 and 4.3 are the snapshots

[2]A binary number generator used in MATLAB, made by *Ronald Aarts*, Mechanical Automation Laboratory, University of Twente.

of the output data of the primary and secondary paths.

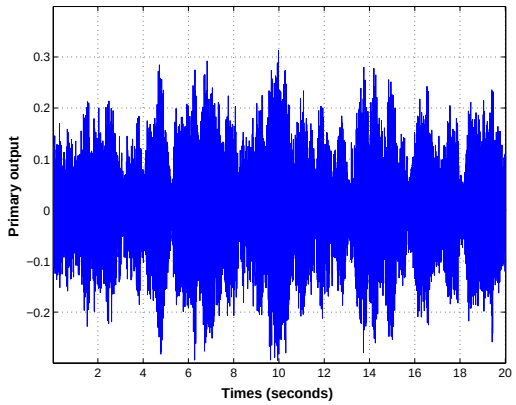

Figure 4.2: *Data snapshot of the output data from the primary path*

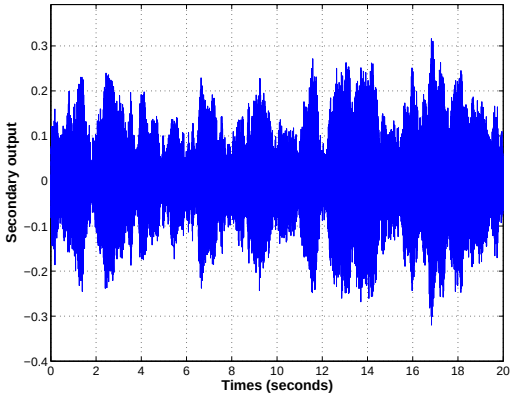

Figure 4.3: *Data snapshot of the output data from the secondary path*

Before identifying the transfer function of the primary and secondary paths with the SMI tool, let's first have a look at the power spectrum density plots of the output data from the primary and secondary paths, as shown in figures 4.4 and 4.5. We have the following important observations:

- We observed resonances at $38\,Hz$ and $98\,Hz$ in both PSD plots, which should correspond to the expected $25\,Hz$ and $80\,Hz$ modes. To find the reason of the mode shifting phenomenon, we recall the structure parameters in table 2.4 and the flexure shape in figure 2.6. One possibility is that the stiffnesses k_1 and k_2 in the one-dimensional setup are stiffer than the expected values, because the effective length of l in the one-dimensional setup may be smaller than what we expected in table 2.4.

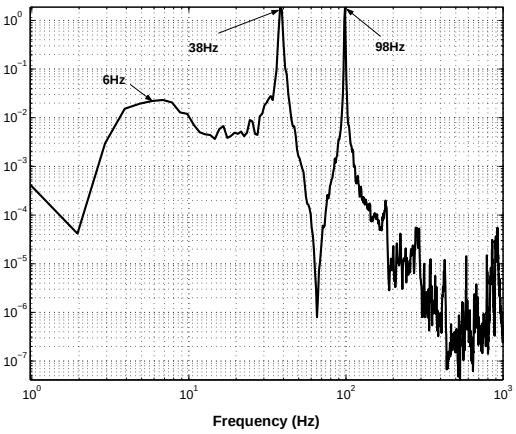

Figure 4.4: *Power spectrum density of the output data from the primary path identification*

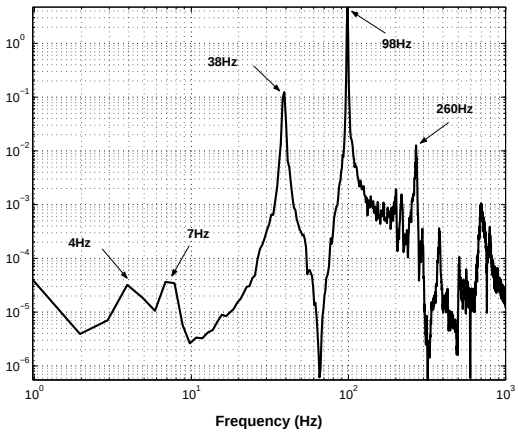

Figure 4.5: *Power spectrum density of the output data from the secondary path identification*

- The expected $3\,Hz$ resonance is difficult to be observed in the secondary path PSD plot. Two possible explanations could be: the $3\,Hz$ mode is highly damped; or the low frequency part is difficult to excite because the secondary path has a very low transmissibility at frequencies below $10\,Hz$.

- The exciter we used for generating the primary disturbance F_f has only unit gain from about $10\,Hz$ (to $20\,kHz$), so the data measured from the primary path at frequencies lower than $10\,Hz$ is mixed with the exciter's dynamics.

- In the real setup, the exciter is rigidly connected to the floor mass M_F, so it is possible that the connection actually increases the moment of inertia of the floor mass. Due to this reason, the lowest irrelevant resonance peak which we expected at $320\,Hz$ is now observed at about $260\,Hz$.

From the spectrum analysis, we can predict that only the frequency components in the output data at frequencies higher than $10\,Hz$ are reliable from our measurement; and the $3\,Hz$ mode might not be found in the identified $P(z)$ and $S(z)$ by the SMI algorithm.

The SMI toolbox allows to identify multi-input & multi-output systems, which means we can have two uncorrelated inputs respectively for the primary path and the secondary path, and identify both of them simultaneously. However, for simplicity reason, the primary and secondary paths are identified separately. The Bode plots of the identified models $\hat{P}(z)$ and $\hat{S}(z)$ are displayed in figures 4.6 and 4.7. Both models are selected with 10^{th} order models. The 10^{th} order models include the expected $38\,Hz$, $98\,Hz$ and $260\,Hz$ resonances, and the low-frequent ($< 10\,Hz$) dynamics cannot be improved by increasing the order of the models.

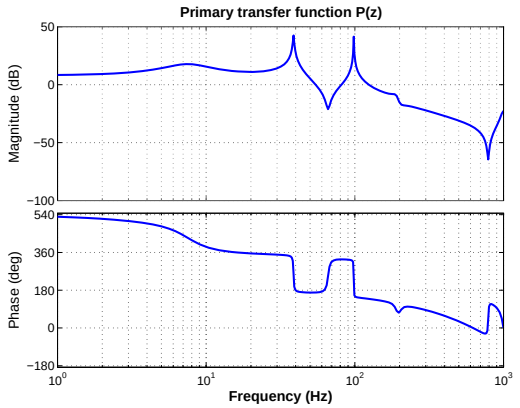

Figure 4.6: *Bode plot of the identified* 10^{th} *order primary path transfer function* $\hat{P}(z)$

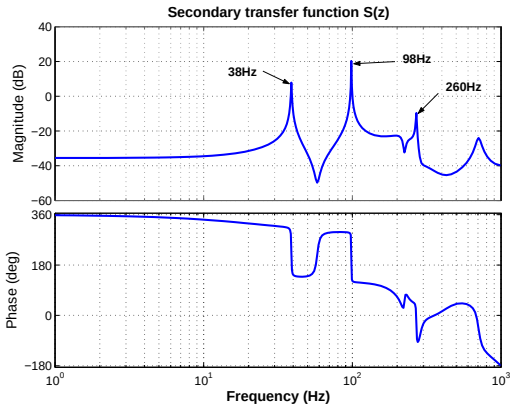

Figure 4.7: *Bode plot of the identified* 10^{th} *order secondary path transfer function* $\hat{S}(z)$

4.1.3 Model validation method

When a model is obtained, a measure is needed to find out how good the model represents the real setup. The model validation procedure in the SMI toolbox is as follows:

Step 1: Split the obtained IO (Input & Output) pair (u, y) into two sets of IO pairs: (u_t, y_t) and (u_v, y_v), of which, (u_t, y_t) is called the training data and (u_v, y_v) is called the validation data.

Step 2: Identify the Linear Time Invariant (LTI) system with (u_t, y_t) using the subspace model identification technique. Then, $y_t(n) = M(z)u_t(n)$, with $M(z)$ the identified system.

Step 3: Use the input data $u_v(n)$ in the validation data as the input of the LTI system $M(z)$, then, $y_e(n) = M(z)u_v(n)$. The quality of the LTI system $M(z)$ is measured by the Variance Accounted For (VAF) value defined as:

$$\mathbf{VAF} = (1 - \frac{var(y_v - y_e)}{var(y_v)}) \times 100\% \tag{4.8}$$

Therefore, the higher the VAF value the better the quality of the identified model. By calculation, the VAF value for the 10^{th} order primary and secondary models are 97.5% and 98.5%. Figures 4.8 and 4.9 are the PSD plots of the validation data y_v and the estimation data y_e for $\hat{P}(z)$ and $\hat{S}(z)$, from which we observe that the mismatch between y_v and y_e in both figures happens only at the low frequencies ($< 20\,Hz$) and the high frequencies ($> 200\,Hz$). Finally, we can conclude that the identified 10^{th} order systems for $\hat{P}(z)$ and $\hat{S}(z)$ well represent the real setup in the frequency range from $20\,Hz$ to $200\,Hz$.

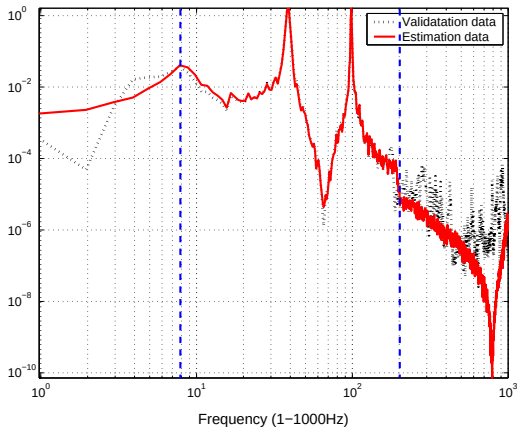

Figure 4.8: *Power spectrum density plot for the validation data y_v and the estimation data y_e for the identified model $\hat{P}(z)$*

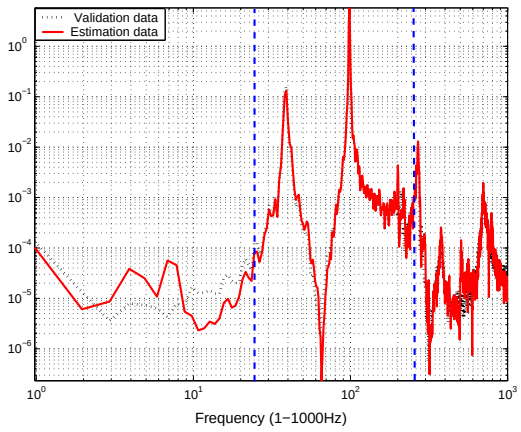

Figure 4.9: *Power spectrum density plot for the validation data y_v and the estimation data y_e for the identified model $\hat{S}(z)$*

Furthermore, as we discussed in chapter 3, the secondary path transfer should be a minimum-phase system, which means $S(z)$ should have all its zeros within the unit circle. Unfortunately, as shown in figure 4.10, the identified secondary path $\hat{S}(z)$ has one

zero[3] out of the unit circle, of which we cannot get rid by changing the model's order. As the minimum-phase is an important property of $\hat{S}(z)$, especially for the application of the adaptive feedforward control strategy, some setup structure changes should be done to solve this problem in further work.

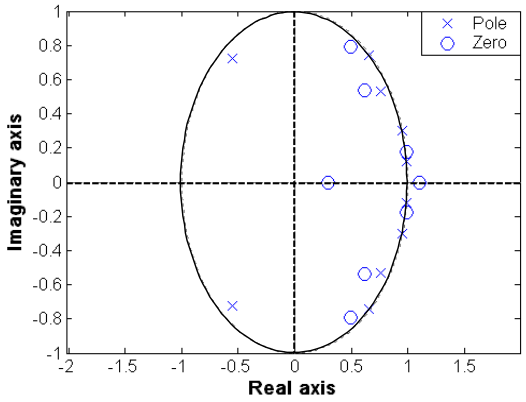

Figure 4.10: *Pole-Zero map of the identified model* $\hat{S}(z)$

4.2 Realtime classic fixed gain feedback control

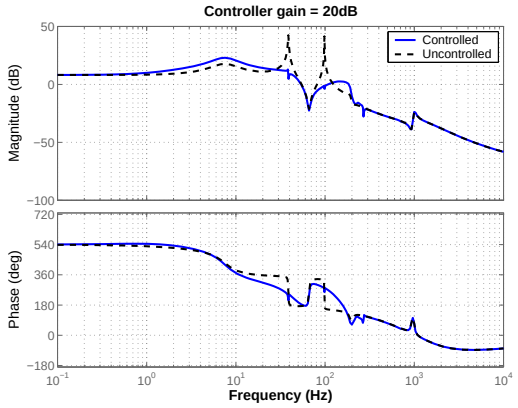

Figure 4.11: *Closed loop control results, controller gain* $= 20dB$

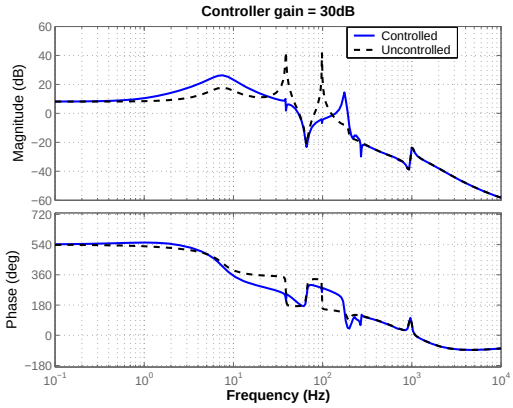

Figure 4.12: *Closed loop control results, controller gain* $= 30dB$

Due to the unexpected non-minimum zeros in the identified secondary path transfer $\hat{S}(z)$, which results in a different phase profile from the model $S(z)$ established in chapter 3, the $+PI+$ fixed gain feedback controller has to change to a $+P+$ controller which only provides a proportional action in the controlled frequency range.

[3]There are two more zeros out of the unit circle, but they are far from the unit circle and only have little effect on the system dynamics.

The closed loop simulation results based on the identified models $\hat{P}(z)$ and $\hat{S}(z)$ using the $+P+$ feedback controller are now available in figures 4.11 and 4.12. Figure 4.11 uses a $20\,dB$ gain controller while figure 4.12 uses $30\,dB$. On one hand, both figures indicate the desired noise reduction at the $38\,Hz$ and $98\,Hz$ resonances. On the other hand, we also observe that the bigger the controller gain is, the more noise reduction is achieved at these two resonant peaks, but the more pump-up happens in the neighborhood frequencies $5 \backsim 20\,Hz$, $110 \backsim 200\,Hz$.

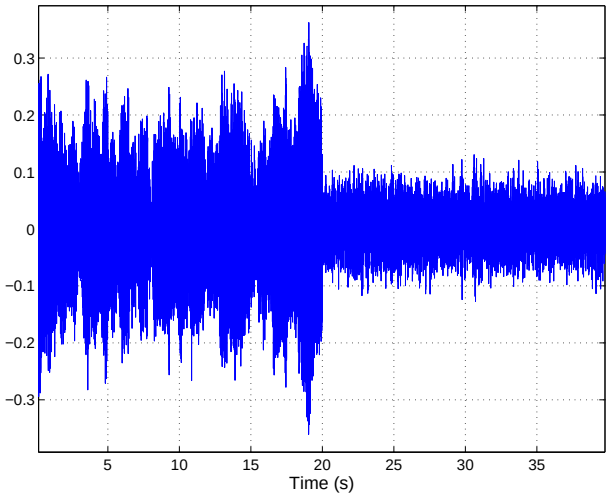

Figure 4.13: *Realtime control: snapshot of the output signal $\ddot{x}_L$, controller turned on at $t = 20s$*

Finally, we implement the controller used in figure 4.11 on the one-dimensional setup. Figure 4.13 is the snapshot of the measured output signal $\ddot{x}_L$ with the controller turned on at $t = 20\,s$. Figure 4.14 is the PSD plot of the data in figure 4.13 with the black dashed curve for the first $20\,s$ data and blue solid curve for the last $20\,s$ data respectively. We obtain about $40\,dB$ and $50\,dB$ noise reduction at the $38\,Hz$ and $98\,Hz$ resonances, and observed the same pump-up phenomenon in the neighborhood region as we detected in the simulation results.

4.3 Summary

This chapter introduced the identification of the primary and secondary paths as well as the realtime experiments on the one-dimensional setup. The definition of the primary path $P(z)$ was changed in the beginning of this chapter. Then, we expended efforts on determining the excitation for the primary and secondary paths such that they can generate the same elongation ($< 25\,\mu m$) for the piezo stacks. We investigated that the secondary path needs more excitation than the primary path, especially in the low frequencies ($< 10\,Hz$).

For the system identification, the binary numbers are used as the input data, the ac-

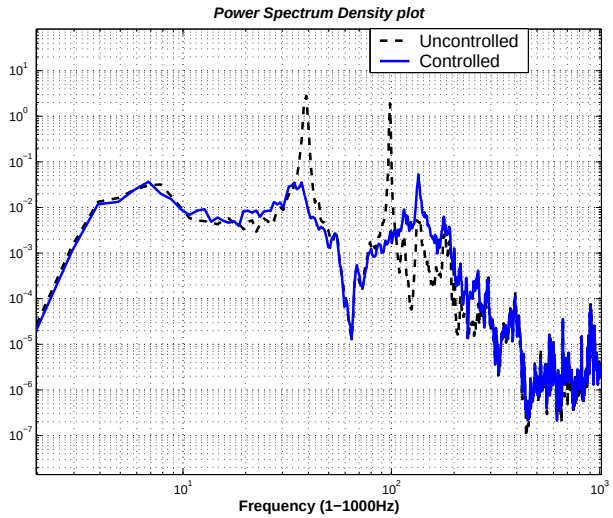

Figure 4.14: *Realtime control results: PSD plots of the output signal $\ddot{x}_L$ with and without control*

celeration of M_L is measured as the output data. The primary and secondary path are identified separately. The spectrum of the output data gave us the following information:

- Low frequencies ($< 10\,Hz$) are hard to excite for both the primary and secondary paths. Because for the primary path, the exciter only has a flat spectrum from about $10\,Hz$, while for the secondary path, the gain of the low frequent ($< 20\,Hz$) transmissibility is too low and the low-frequent dynamics of $S(z)$ are hardly excited.
- The expected $25\,Hz$ and $80\,Hz$ modes now move to $38\,Hz$ and $98\,Hz$ in the real setup. The reason might be that the stiffnesses k_1 and k_2 are higher in the real setup than we calculated.
- The lowest irrelevant resonance which we expected to be above $320\,Hz$ is now at $260\,Hz$ in the real setup probably due to the rigid connection between the exciter and the floor mass M_F.

Followed by the spectrum analysis, we identified the primary transfer $\hat{P}(z)$ and secondary transfer $\hat{S}(z)$ both with 10^{th} order models by using the subspace model identification tools. Model validation shows these two 10^{th} order models have 97.5% and 98.5% VAF values for the primary and secondary paths respectively. Furthermore, we found that the identified $\hat{P}(z)$ and $\hat{S}(z)$ well fit with the real setup at frequencies $20 \backsim 200\,Hz$. Another notice is that the identified secondary path transfer function $\hat{S}(z)$ has zeros out of the unit circle. For further adaptive feedforward control purpose, some structure modifications are needed to get rid of these non-stable zeros.

The last part of this chapter was the realtime experiment results by applying the classic fixed gain feedback control on the one-dimensional setup. Due to the unexpected non-minimum zeros in the identified secondary path $\hat{S}(z)$, the $+PI+$ controller designed in

the previous chapter had to change to a $+P+$ controller. Finally, about $40\,dB$ and $50\,dB$ noise reduction were achieved at the $38\,Hz$ and $98\,Hz$ resonances respectively by applying the designed $+P+$ controller on the one-dimensional setup.

Chapter 5

Conclusions and recommendations

5.1 Conclusions

The goal of the project is to design and build up a one-dimensional demonstration setup for vibration suppression of high-precision machines by the active hard mounting technique. The design started with building the ideal physical model of a hard-mounted positioning machine and determining the dominant machine suspension modes. We found that the machine's supporting and internal suspensions are the dominant suspension modes for the positioning machine and chose these two resonances respectively at $25Hz$ and $80Hz$. Additionally, a $3Hz$ resonance is designed to reflect the floor suspension. The setup parameters were determined by mechatronic approach and examined by modal analysis. The structure of the setup was discussed later on, with special attention to the means to realize the one dimensional motion.

We introduced three active vibration control strategies: the adaptive feedforward control using the MFxLMS algorithm, classic fixed gain feedback control using a $+PI+$ controller, and induced mode feedback control. Simulation results showed that the adaptive feedforward control provides broadband noise reduction, while the other two feedback solutions installed *artificial damping* at the expected resonances. The feedback $+PI+$ control scheme is actually a velocity feedback strategy based on the acceleration measurements, while the induced mode control makes the controlled system to mimic the vibration attenuation performance of an ideal passively isolated system. These two feedback solutions gave similar simulation results, but the induced mode control scheme has the advantage of gaining control action and saving energy for the piezo-actuator in the low frequency range.

Identification of the one-dimensional setup was done with the Subspace Model Identification technique. The spectrum of the output data from the primary and secondary paths gave us some helpful information: 1) Only the information from the spectrums above $10\,Hz$ is reliable from both the primary and secondary path identifications; 2) The expected supporting and internal modes at $25Hz$ and $80Hz$ shifted to $38Hz$ and $98Hz$ in the real setup, possibly because stiffer k_1 and k_2 are used. Later on, the primary path and

secondary path were both identified with a 10^{th} order model, for which the VAF values are 97.5% and 98.5% respectively. Further spectrum analysis of the validation data and estimation data indicated a nice fitting between the identified models and the real setup in the frequencies from $20\,Hz$ to $200\,Hz$. The realtime experiments of implementing the fixed gain feedback controller showed $40\,dB$ and $50\,dB$ noise reduction at the supporting mode and internal mode respectively.

5.2 Recommendations

Following are some suggestions for further work on the one-dimensional setup:

- The supporting and internal suspension modes in the real setup are shifted higher than we expected. One possible reason is that the stiffnesses k_1 and k_2 are stiffer than we calculated. Although the mode-shift will not make any difference for control purpose, change of k_1 and k_2 may help us to achieve the original goal.

- The primary path exciter has a flat spectrum from about $10\,Hz$ (to $20\,kHz$). As the ultra intention of the *SMART MOUNT* project is to suppress the vibrations as low as from $1\,Hz$, using another exciter is necessary to provide enough excitation in the low frequency range.

- The definition of the input of the primary path is suggested to be the acceleration of the floor mass M_L, because in reality, it is not possible to directly measure the excitation of the ground.

- From the realtime control results, we get promising noise attenuation results at the two resonances as we expected. However, the phenomenon that with the feedback strategy, the more damping achieved at the resonance, the more pump-up we get in the neighborhood frequency range is interesting to be investigated in further research.

- The minimum-phase property of $\hat{S}(z)$ is an essential concept for the adaptive feedforward control strategy. One possibility that the estimated secondary path transfer function $\hat{S}(z)$ had zeros out of the unit circle is that, the guiding flexures were prestressed in the one-dimensional setup (because the diameter of the guiding flexure is a bit bigger than the inner diameter of the transparent tube), which resulted in a *negative stiffness*, consequently the non-minimum zeros. As a result, a careful modification of the size of the guiding flexures might help to persist the minimum-phase property of the secondary path transfer function.

- Another advantage of using the induced mode control strategy is that a sky-hook damper could be used as the ideal passively isolated system, such that instead of a $-20\,dB$ slope attenuation in the simulation results we obtained in chapter 3, the sky-hook damper could gain a $-40\,dB$ slope noise reduction.

Appendix A

Technical Equipment

- **Sensor Amplifier:**
  Brüel & Kjær Nexus conditioning amplifier 2692
  `Experiment settings:`
  Output sensitivity: $3.16\,V/ms^{-2}$
  Built-in low-pass filter: $1\,kHz$
  Built-in high-pass filter: $0.1\,Hz$

- **Sensor:**
  Brüel & Kjær 4381
  Reference sensitivity: $10.1\,pC/ms^{-2}$ (at $159.2\,Hz$, $20\,ms^{-2}$ RMS and $24\,^{\circ}$C)
  Lower frequency limit: determined by the amplifier used
  Upper frequency limit: $4.8\,kHz$
  Piezoelectric material: P23 (Delta shear)

- **Piezo Amplifier:**
  Piezomechanick SVR 150/3
  `Experiment settings:`
  Offset: $60\,V$
  Amplification: $\pm 5\,V$

- **Piezo actuator:**
  Piezomechanik PSt 150/5/40 VS10
  Max. stroke: $50\,\mu m$
  Length: $46\,mm$
  Stiffness: $12 \times 10^6\,N/m$
  Resonance frequency: $20\,kHz$

- **Shake:**
  Vibration exciter Brüel & Kjær 4809
  Frequency range: $10\,Hz \backsim 20\,kHz$

Coil resistance: $2\,\Omega$ approx.
Force constant: $6.4\,N/A$

- **Shaker Amplifier:**
  Brüel & Kjær 2706
  `Experiment settings:`
  Amplification: 1

- **d-Space System:**
  d-Space 1105 system

- **Computer:**
  Desktop Pentium 4: $3.0\,GHz$ CPU, $1\,Gb$ internal memory

Appendix B

Technical Drawings

List of drawings:

- Assembly plot
- Guiding flexure
- Flexure used to realize the stiffness of $1.2 \times 10^5\, N/m$
- Flexure used to realize the stiffness of $3 \times 10^5\, N/m$
- Top mass and middle mass
- Bottom mass

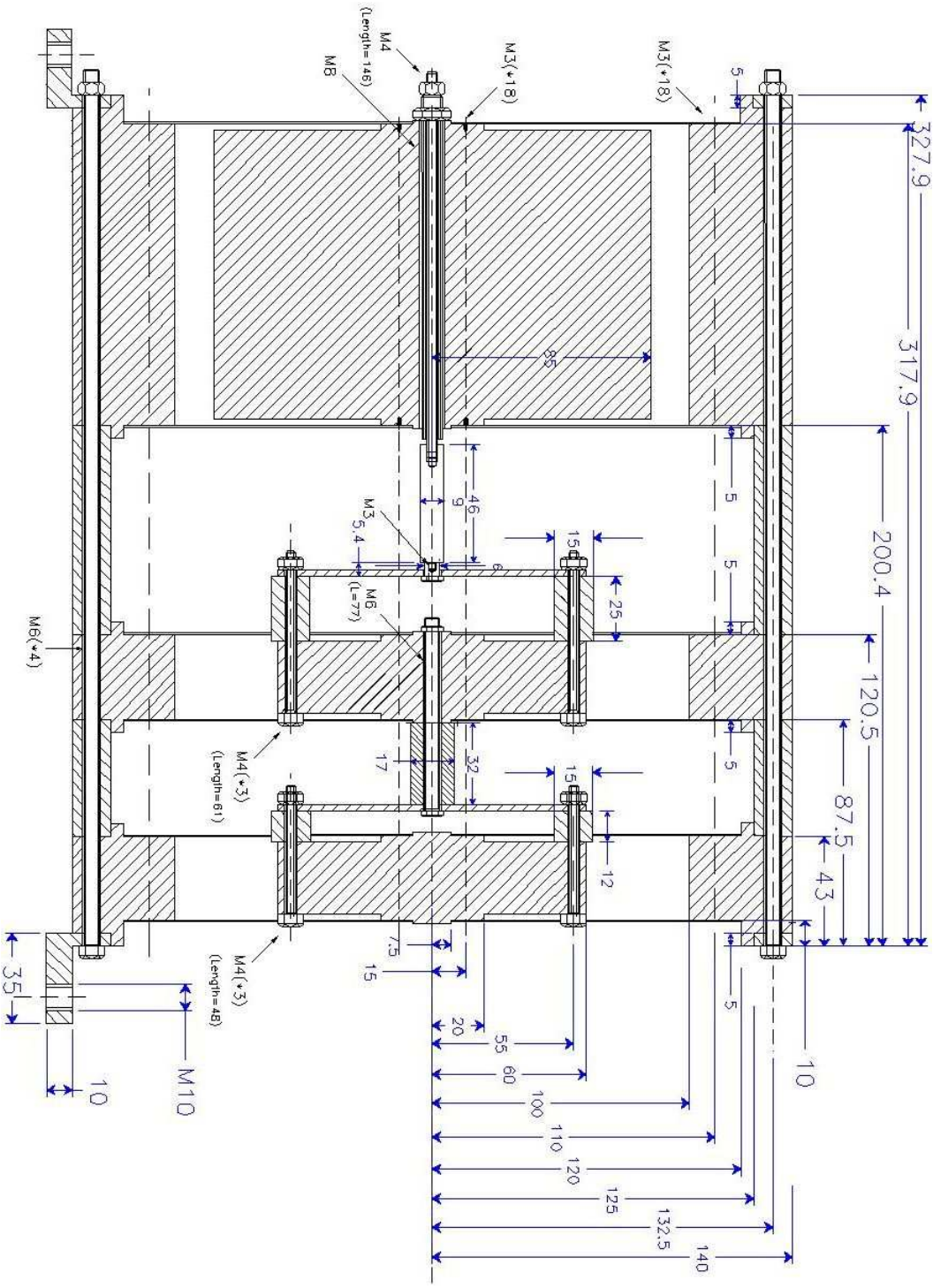

Figure B.1: *Assembly plot*

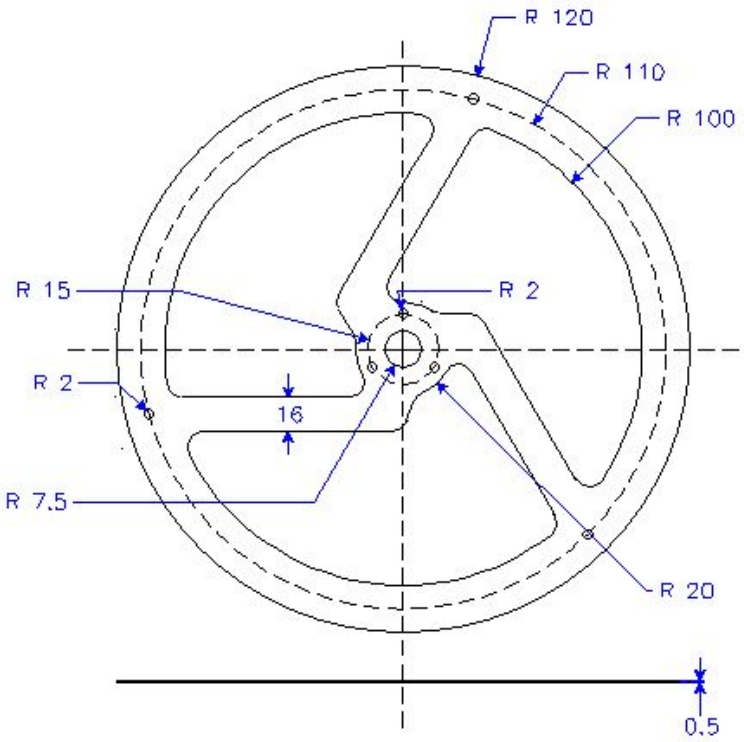

Figure B.2: *Guiding flexure*

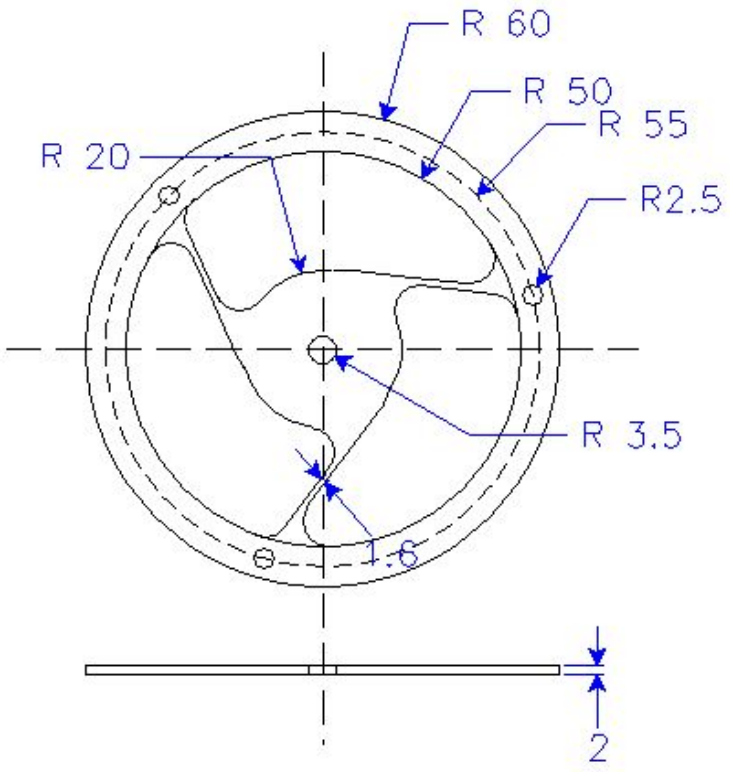

Figure B.3: *Flexure for* $k_1 = 1.2 \times 10^5\, N/m$

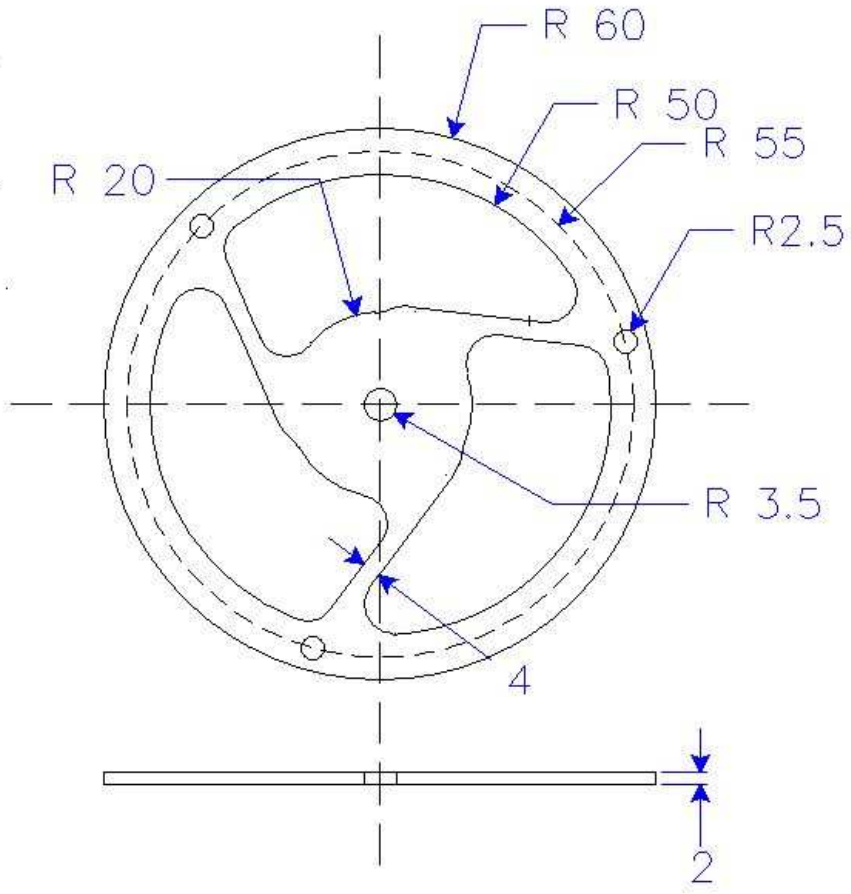

Figure B.4: *Flexure for* $k_2 = 3 \times 10^5\, N/m$

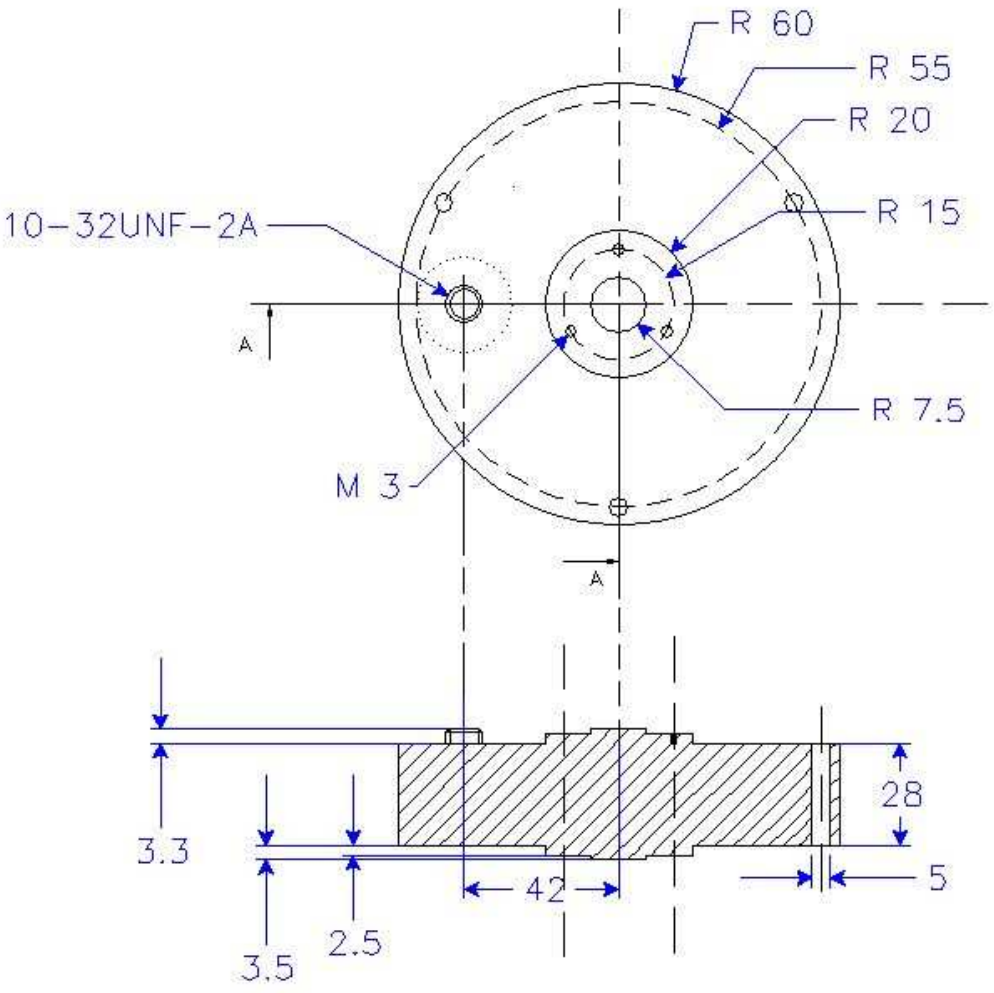

Figure B.5: *Top mass and middle mass*

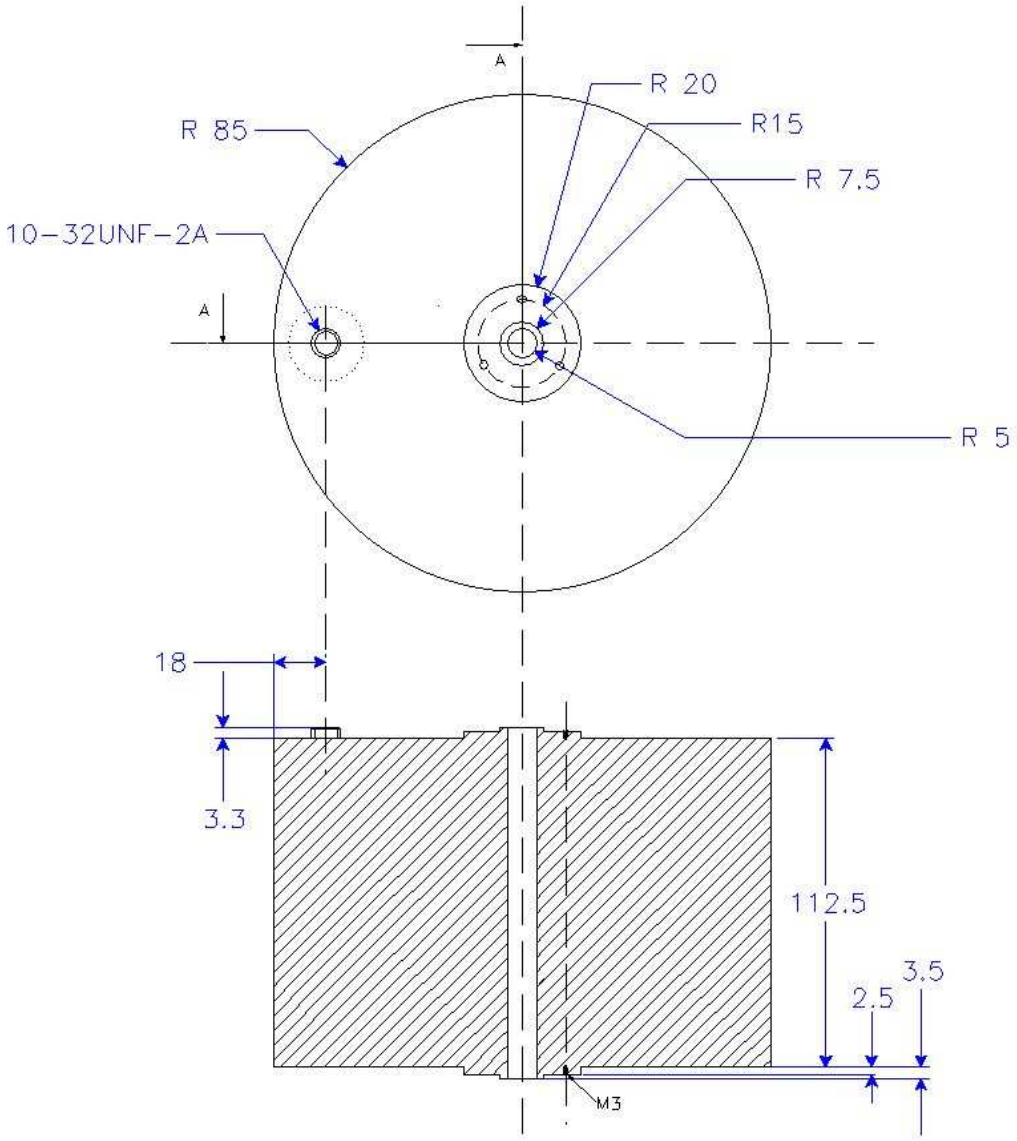

Figure B.6: *Bottom mass*

Bibliography

[1] Rijs R.M.G., *Floorvibrations: Measurements and Specifications*, Philips Electronics Netherlands, B.V., Eindhoven, 2004.

[2] *Technical Background Brochure*, TMC, *website:* www.techmfg.com.

[3] Inman D. J., *Engineering Vibration*, Prentice Hall, 2001.

[4] Howell L. L., *Compliant Mechanisms*, Wiley-Interscience Publication, 2001.

[5] Elliott, S.J., *Signal processing for active control*, Academic Press, 2001.

[6] Kuo, S.M., *Active noise control systems*, John Wiley & Sons, Inc., 1996.

[7] Cock, K. de, Moor, B. de, Leuven, K.U., *Subspace identification methods*, Department of Electrical Engineering (ESAT SCD), Leuven.

[8] Nijsse, G., Super, H., Dijk, J. van, Jonker, J.B., *Subspace based identification and control of a six-degreesof-freedom vibration isolation set-up*, University of Twente, Faculty of Engineering Technology, Department of Mechanical Engineering, Mechanical, Automation Laboratory, 2003.

[9] Yu F., Bouchard M., *Multichannel active noise control algorithms using inverse filter*, University of Ottawa.

[10] Hagedoorn, W., *Design and identification of a six degrees of freedom vibration isolation setup*, Masters thesis, University of Twente, Faculty of Engineering Technology, Department of Mechanical Engineering, Laboratory of Mechanical Automation, report number WA 850.

[11] Holterman, J., *Vibration control of High-Presicion Machines with Active Structural Elements*, Twente University Press, PhD thesis, University of Twente, 2002.

[12] *Piezo-mechanics: an introduction*, Piezomechanic GmbH, Germany, *website:* www.piezomechanic.com, 2003.

[13] Petersen C.D., *Controlling broadband disturbances on a one-degree-of-freedom experimental vibration isolation set-up*, Masters thesis, University of

Twente, Faculty of Engineering Technology, Department of Mechanical Engineering, Laboratory of Mechanical Automation, report number WA 0888.